Stockholm University

Structure determination of beam-sensitive materials by 3D electron diffraction

From pharmaceuticals to porous materials

Jiaoyan Xu

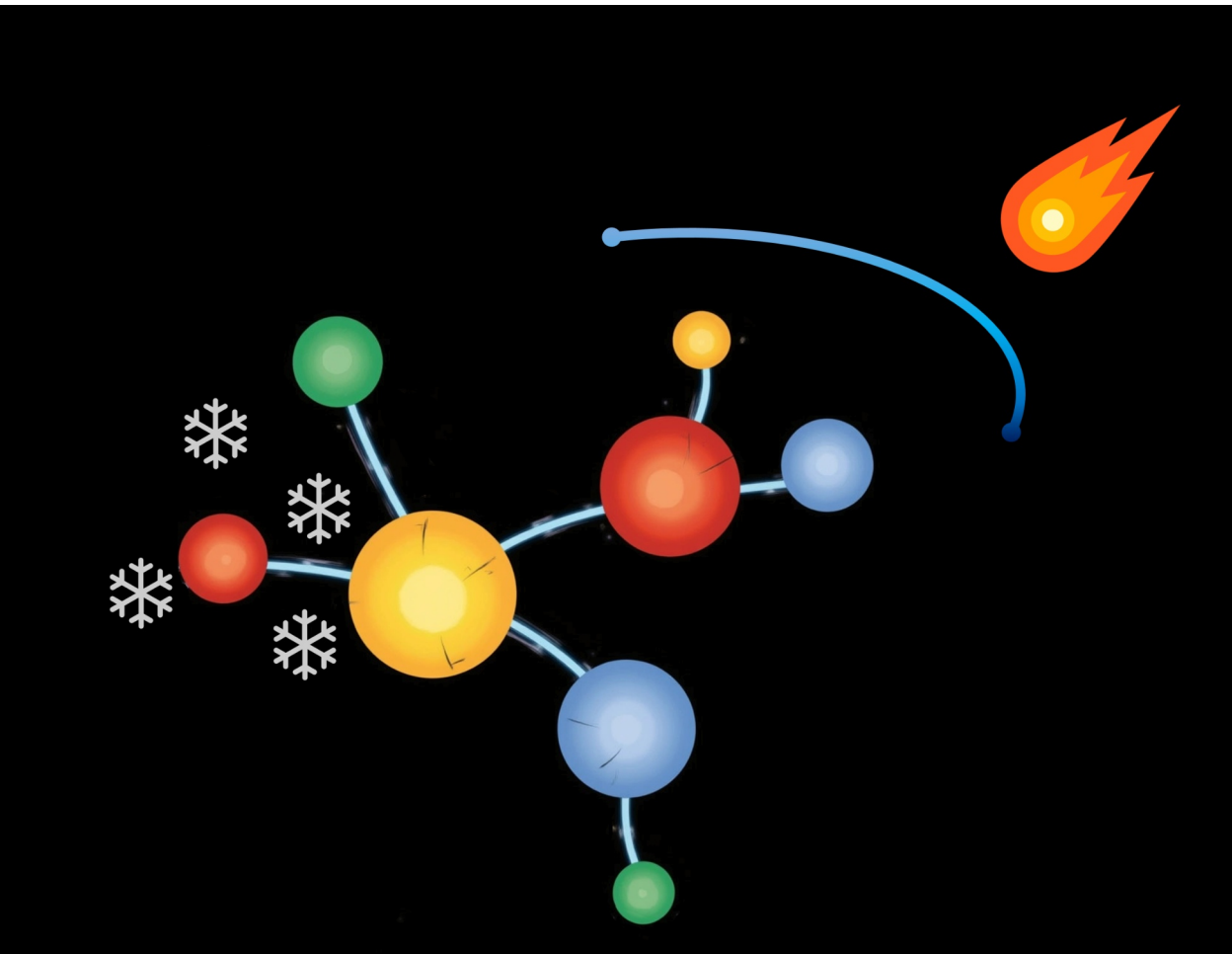

Doctoral Thesis in Physical Chemistry at Stockholm University, Sweden 2025

Structure determination of beam-sensitive materials by 3D electron diffraction

From pharmaceuticals to porous materials

Jiaoyan Xu

Academic dissertation for the Degree of Doctor of Philosophy in Physical Chemistry at Stockholm University to be publicly defended on Friday 16 May 2025 at 09.00 in Magnéli Hall, Svante Arrhenius väg 16.

Abstract

Three-dimensional electron diffraction (3DED) has become a powerful method for structure determination of nano-/micron-sized crystalline materials. Due to their negative charge, electrons interact with both atomic nuclei and surrounding electron clouds in matter. While this strong interaction enables the study of nano-/micron-sized crystals, it also induces electron-beam damage during 3DED experiments. When electrons interact with a crystal, they can cause atomic displacement and bond breakage, which affects the structure and/or the chemistry of the specimen. This damage poses a significant challenge for 3DED studies of beam-sensitive materials.

In this thesis, eight beam-sensitive crystalline materials were investigated using 3DED, including pharmaceuticals, zeolites, and metal-organic frameworks (MOFs). To address electron-beam damage, several data acquisition strategies were developed to preserve beam-sensitive materials during 3DED experiments. These strategies include: 1) using low electron fluence, 2) cryo-cooling, and 3) the low-dose cryo-cRED (cryogenic continuous rotation electron diffraction) method, which combines the former two. These strategies reduce electron-beam damage and enhance the reliability of 3DED.

Additionally, a glovebox-assisted sample preparation workflow was developed to prepare cryo-samples under a controlled atmosphere. This approach enables 3DED studies of beam-sensitive materials that are also sensitive to air.

Using 3DED at room temperature, two new piroxicam (PXM) polymorphs were identified. To mitigate electron-beam damage, the cumulative electron fluence per dataset was reduced by adjusting data acquisition parameters related to electron flux and recording time. The structure information provided insight into the structure–property relationship between hydrogen bonding and melting point. Furthermore, the structure of anhydrous sodium valproate was determined for the first time using 3DED. To address its sensitivity to both electrons and moisture, a glovebox was used to preserve the anhydrous structure during the cryo-sample preparation. Cryogenic cooling was then employed during data collection to reduce electron-beam damage.

Moreover, the structure of ZMQ-1, the first stable meso-microporous aluminosilicate zeolite, was uncovered using 3DED. To determine the position of the organic structure-directing agents (OSDAs), the low-dose cryo-cRED method was employed to stabilize OSDA molecules against electron-beam damage. Likewise, three isostructural aluminum(III)-monocarboxylates (CAU-71-X, where X = Ac, Prop, and TGA), were studied using low-dose cryo-cRED. This combined method stabilized the highly flexible ligands, enabling both structure determination and positional disorder refinement of the CAU-71 compounds.

Keywords: *3D electron diffraction, structure determination, beam-sensitive material, electron-beam damage, humidity-sensitive sample, glovebox-assisted sample preparation, pharmaceuticals, zeolites, metal-organic frameworks, polymorphism.*

Stockholm 2025
http://urn.kb.se/resolve?urn=urn:nbn:se:su:diva-241607

ISBN 978-91-8107-198-6
ISBN 978-91-8107-199-3

Department of Chemistry

Stockholm University, 106 91 Stockholm

STRUCTURE DETERMINATION OF BEAM-SENSITIVE MATERIALS BY 3D ELECTRON DIFFRACTION

Jiaoyan Xu

Stockholm University

Structure determination of beam-sensitive materials by 3D electron diffraction

From pharmaceuticals to porous materials

Jiaoyan Xu

ISBN print 978-91-8107-198-6
ISBN PDF 978-91-8107-199-3

Printed in Sweden by Universitetsservice US-AB, Stockholm 2025

To my family.

Doctoral Thesis 2025
Department of Chemistry
Stockholm University, Sweden

Faculty opponent:
Christian W. Lehmann
Max-Planck-Institut für Kohlenforschung, Germany

Evaluation committee:
Chao Xu
Department of Materials Science and Engineering
Uppsala University, Sweden

Gulaim Seisenbaeva
Department of Molecular Sciences
Swedish University of Agricultural Sciences (SLU), Sweden

Gunnar Svensson
Department of Chemistry
Stockholm University, Sweden

Substitute:
Mårten Ahlquist
Theoretical Chemistry and Biology
KTH, Sweden

Abstract

Three-dimensional electron diffraction (3DED) has become a powerful method for structure determination of nano-/micron-sized crystalline materials. Due to their negative charge, electrons interact with both atomic nuclei and surrounding electron clouds in matter. While this strong interaction enables the study of nano-/micron-sized crystals, it also induces electron-beam damage during 3DED experiments. When electrons interact with a crystal, they can cause atomic displacement and bond breakage, which affects the structure and/or the chemistry of the specimen. This damage poses a significant challenge for 3DED studies of beam-sensitive materials.

In this thesis, eight beam-sensitive crystalline materials were investigated using 3DED, including pharmaceuticals, zeolites, and metal-organic frameworks (MOFs). To address electron-beam damage, several data acquisition strategies were developed to preserve beam-sensitive materials during 3DED experiments. These strategies include: 1) using low electron fluence, 2) cryo-cooling, and 3) the low-dose cryo-cRED (cryogenic continuous rotation electron diffraction) method, which combines the former two. These strategies reduce electron-beam damage and enhance the reliability of 3DED.

Additionally, a glovebox-assisted sample preparation workflow was developed to prepare cryo-samples under a controlled atmosphere. This approach enables 3DED studies of beam-sensitive materials that are also sensitive to air.

Using 3DED at room temperature, two new piroxicam (PXM) polymorphs were identified. To mitigate electron-beam damage, the cumulative electron fluence per dataset was reduced by adjusting data acquisition parameters related to electron flux and recording time. The structure information provided insight into the structure–property relationship between hydrogen bonding and melting point. Furthermore, the structure of anhydrous sodium valproate was determined for the first time using 3DED. To address its sensitivity to both electrons and moisture, a glovebox was used to preserve the anhydrous structure during the cryo-sample preparation. Cryogenic cooling was then employed during data collection to reduce electron-beam damage.

Moreover, the structure of ZMQ-1, the first stable meso-microporous aluminosilicate zeolite, was uncovered using 3DED. To determine the position of the organic structure-directing agents (OSDAs), the low-dose cryo-cRED method was employed to stabilize OSDA molecules against electron-beam

damage. Likewise, three isostructural aluminum(III)-monocarboxylates (CAU-71-X, where X = Ac, Prop, and TGA), were studied using low-dose cryo-cRED. This combined method stabilized the highly flexible ligands, enabling both structure determination and positional disorder refinement of the CAU-71 compounds.

Keywords: 3D electron diffraction, structure determination, beam-sensitive material, electron-beam damage, humidity-sensitive sample, glovebox-assisted sample preparation, pharmaceuticals, zeolites, metal-organic frameworks, polymorphism.

List of publications

This thesis is based on the following papers:

Paper I:

Polyethylene Glycol-Assisted Melt Crystallization of Two New Piroxicam Polymorphs Revealed by 3D Electron Diffraction

Jiaoyan Xu†, Changlin Yao†, Shufang Zhang, Xiaodong Zou, Yue Gui, Lei Wang, and Hongyi Xu, *Crystal Growth & Design* **2024** *24* (17), 7298-7305

Scientific contribution: I was responsible for the structure determination of both piroxicam polymorphs, Forms VIII and IX. I carried out all experimental work of 3DED and made major contributions to the writing of the manuscript.

Paper II:

Unveiling the Structure of Anhydrous Sodium Valproate with 3D Electron Diffraction and a Facile Sample Preparation Workflow

Jiaoyan Xu, Vivek Srinivas, Rohit Kumar, Laura Pacoste, Yiwang Guo, Taimin Yang, Changquan Calvin Sun, Martin Högbom, Xiaodong Zou and Hongyi Xu. *ChemRxiv. 2025; doi:10.26434/chemrxiv-2025-8qxqp. Submitted to ACS Central Science.*

Scientific contribution: I was responsible for the structure determination of anhydrous sodium valproate. I developed a glovebox-assisted sample preparation workflow to preserve its anhydrous structure under humidity-free atmosphere during plunge freezing. I carried out all experimental work and made major contributions to the writing of the manuscript.

Paper III:

A stable zeolite with atomically ordered and interconnected mesopore channel

Peng Lu†, Jiaoyan Xu†, Yiqing Sun†, Rémy Guillet-Nicolas, Tom Willhammar, Mohammad Fahda, Eddy Dib, Bo Wang, Zhengxing Qin, Hongyi Xu, Jung

Cho, Zhaopeng Liu, Haijun Yu, Xiaobo Yang, Qiaolin Lang, Svetlana Mintova, Xiaodong Zou & Valentin Valtchev, *Nature* **636**, 368–373 (2024).

Scientific contribution: I was responsible for the structure determination of both as-made and calcined ZMQ-1. I determined the positions of OSDAs within the as-made sample using low-dose cryo-cRED method. I made major contributions to the writing of the 3DED section and structural analysis in the manuscript.

Paper IV:

Isostructural Aluminum (III) Monocarboxylate Metal–Organic Frameworks built from 18-ring Honeycomb Layers

Bastian Achenbach[†], Jiaoyan Xu[†], Zheting Chu, Xiaodong Zou, Norbert Stock. *In manuscript.*

Scientific contribution: I was responsible for the structure determination of three CAU-71-X compounds. I carried out all experimental work of 3DED and made major contributions to the writing of the 3DED section and structural analysis in the manuscript.

[†] Authors contributed equally to the paper.
Preprints were made with permission from the publishers.

Papers not included in this thesis:

1. Lightowler, M., Li, S., Ou, X., Cho, J., Liu, B., Li, A., Hofer, G., Xu, J., Yang, T., Zou, X., Lu, M., & Xu, H. (2024). Phase Identification and Discovery of an Elusive Polymorph of Drug-Polymer Inclusion Complex Using Automated 3D Electron Diffraction. *Angewandte Chemie International Edition*, *63*(16), e202317695.
Scientific contribution: I contributed to the data collection and sample preparation for this study.

2. Wang, R., Zou, H., Zheng, R., Feng, X., Xu, J., Shangguan, Y., … Chen, H. (2022). Molecular Dynamics beyond the Monolayer Adsorption as Derived from Langmuir Curve Fitting. *Inorganic Chemistry, 61*(20), 7804–7812.
Scientific contribution: I contributed to the experimental design and writing the manuscript.

Content

Abbreviations

3DED	Three-dimensional Electron Diffraction
PCP	Porous coordination polymer
PXM	Piroxicam
ZMQ-1	Zeolitic Materials, Qingdao Institute of Bioenergy and Bioprocess Technology, No. 1
OSDA	Organic structure-directing agent
CAU-71-X	Christian-Albrechts-University-71-X[i]
-Ac	Acetate ligand
-Prop	Propionate ligand
-TGA	Thioglycolate ligand
SCXRD	Single-crystal X-ray diffraction
PXRD	Powder X-ray Diffraction
TEM	Transmission electron microscope
ADT	Automated Diffraction Tomography
RED	Rotation electron diffraction
MicroED	Microcrystal electron diffraction
IEDT	Integrated electron diffraction tomography
cRED	Continuous Rotation Electron Diffraction
LN_2	Liquid nitrogen
cryo-EM	Cryogenic electron microscopy
REDp	Rotation ED processing software
XDS	X-ray detector software package
AutoLEI	Automated Real-time and offline batch 3DED/MicroED data processing Graphic User Interface
GooF	Goodness-of-Fit
ADPs	Atomic displacement parameters

[i] X represents the ligand.

osf	Overall scale factor
sof	Site occupancy factors
PEG	Polyethylene Glycol
BF images	Bright-field images
T-atoms	Tetrahedral atoms
iDPC	Integrated Differential Phase Contrast
ADF	Annular Dark Field
STEM	Scanning Transmission Electron Microscopy
Cryo-cRED	Cryogenic continuous rotation electron diffraction

1. Introduction and aim of the thesis

The physicochemical properties of substances govern their behavior, performance, and potential applications. Understanding these properties enables researchers to design materials, optimize synthesis and improve their performance. In the case of crystalline materials, these properties are primarily related to their crystal structures.[1] Therefore, accurate structure determination is crucial for gaining fundamental insights and promoting practical applications.

Various diffraction techniques have been developed for crystal structure determination, including X-ray diffraction, neutron diffraction, and electron diffraction (ED). Among these, X-ray diffraction remains the most widely used technique for analyzing crystalline structures.[2,3] The two primary X-ray diffraction methods, single-crystal X-ray diffraction (SCXRD) and powder X-ray diffraction (PXRD), each have distinct strengths and limitations. SCXRD has long been regarded as the gold standard for structure determination of crystalline materials; however, it has strict requirements for crystal quality and size (typically larger than 5 μm in each dimension).[4,5] For many materials, obtaining large single crystals with high crystallinity can be time-consuming or even impossible. Although PXRD is capable of analyzing nano-sized samples[6], it suffers from peak overlapping. For well-crystallized samples, peak overlapping arises because PXRD pattern compresses three-dimensional diffraction data into one dimension, causing previously distinguishable reflections to merge. This complicates the peak indexing and intensity integration, limiting the application of PXRD in structure determination. For samples with defective crystals, solving the structure from PXRD data becomes even more challenging.

Given these limitations, three-dimensional electron diffraction (3DED) offers a promising solution.[7] 3DED encompasses several techniques that share the same core concept: sampling the available 3D reciprocal space by rotating the crystal around an arbitrary axis under an electron beam.[8] As a natively charged particle, electrons interact with matter through Coulombic forces, engaging both the positively charged atomic nuclei and the surrounding electron clouds. In contrast to X-ray diffraction, which primarily involves the interaction between X-rays and the electron clouds, electrons exhibit much stronger interaction with matter. By using electrons for diffraction, 3DED enables the structure determination of micron- and even nano-sized crystals, particularly those too small for SCXRD or too complex for PXRD.[9] To date, 3DED has been successfully employed in the structural analysis of various materials, ranging from inorganic compounds to complex macromolecules.[10–13]

Despite its success, the strong interaction between electrons and matter also introduces challenges to the structural analysis: electron-beam damage.[14,15] Electron-beam damage refers to the structural and chemical changes of a specimen induced by incident electrons, which can compromise the accuracy of structure determination. Fundamentally, electron-matter interactions can be classified into elastic scattering and inelastic scattering.[16] Elastic scattering, where the incident electrons are scattered by specimen without energy loss, contributes to the diffraction pattern in 3DED. In contrast, inelastic scattering involves energy transfer between incident electrons and specimen atoms, which can trigger atomic displacement, bond breaking and mass loss. These side effects of inelastic scattering are collectively referred to as electron-beam damage, which presents a significant challenge for 3DED analysis of beam-sensitive materials.

Beam-sensitive materials encompass a wide range of materials that are highly vulnerable to electron-beam damage.[17–19] These materials typically contain light elements, weak chemical bonds, or volatile components, making them prone to structural degradation and phase transformation under electron irradiation. As a result, the structural integrity of these materials may be compromised during 3DED experiments, necessitating the development of strategies to minimize the electron-beam damage.

The mechanisms of electron-beam damage are complex and vary between materials.[20,21] There are three primary damage mechanisms: 1) radiolysis, 2) heating effects, and 3) knock-on damage. Radiolysis, which primarily occurs through electron-electron interactions such as ionization, leads to the breaking of chemical bonds in materials. Heating occurs when phonons are generated by inelastic scattering, leading to localized temperature increases in the specimen. Knock-on damage involves the displacement of atoms from the crystal lattice by incident electrons. One way to alleviate beam damage is to use the highest available accelerating voltage, which reduces the probability of inelastic scattering events; however, this approach also aggravates knock-on damage. An alternative method is cooling the specimen to cryogenic temperatures, which lessens the heating effect to some extent. This method, labelled as cryo-cooling in this thesis, uses liquid nitrogen to cool the sample to approximately 95 K.[22] Another solution involves acquiring 3DED data under threshold electron fluence, which protects samples that are sensitive to the cumulative electron fluence.[23] In some cases, the latter two strategies are combined to minimize electron-beam damage, which is referred to as low-dose cryo-cRED[24] in this thesis.

Along with the challenges posed by electron sensitivity, other properties of the samples present additional difficulties for practical 3DED analysis of beam-sensitive materials. As presented in Section 3.1.2 of Chapter 3, the

hygroscopicity of beam-sensitive sodium valproate makes it prone to absorbing moisture from the air during sample preparation. To preserve its anhydrous structure, a nitrogen-regulated glovebox with a designed cooling chamber was employed to provide a humidity-free atmosphere for plunge freezing. Based on this setup, a glovebox-assisted sample preparation workflow was developed to prepare cryo-samples under a controlled atmosphere.

This thesis aims to push the boundaries of 3DED analysis for beam-sensitive crystalline materials. This is achieved through the development of data acquisition strategies and a tailored sample preparation workflow, which can stabilize the crystalline structure and reduce electron-beam damage during 3DED experiments. The thesis is organized into seven chapters. The first three chapters provide research background, theories, and experimental details involved in this thesis. Chapter 2 provides a brief introduction to electron crystallography, 3DED techniques, electron-beam damage, and beam-sensitive materials. Chapter 3 details the experimental procedures for 3DED, including sample preparation, data collection, data processing, structure solution, and structure refinement.

Chapter 4 presents two structural studies of pharmaceutical materials: piroxicam (PXM) and anhydrous sodium valproate. The 3DED experiment of PXM was carried out at room temperature. To alleviate the electron-beam damage, data acquisition parameters were carefully adjusted to reduce the cumulative electron fluence per dataset. Since electron fluence is the product of electron flux and recording time, both factors were carefully adjusted in practice. The electron flux was controlled by selecting suitable condenser apertures and tuning the spot size via adjustments of the condenser lens. The recording time was modified by changing the rotation speed, and rotation range. In contrast, the crystalline structure of anhydrous sodium valproate was found to be sensitive to both electron and moisture. To preserve its anhydrous structure during plunge freezing, a glovebox-assisted workflow was developed to enable plunge freezing under a humidity free nitrogen atmosphere. Subsequently, the cryo-cooling was used to protect samples from electron-beam damage during data collection.

Chapter 5 presents two structural analyses of two porous materials: zeolite (ZMQ-1) and porous coordination polymer (CAU-71-X). ZMQ-1 is the first stable aluminosilicate zeolite with an intersecting intrinsic meso-microporous channel system. The framework structures of both as-made and calcined ZMQ-1 were successfully determined using 3DED data collected at room temperature. However, due to the electron-beam damage, the position of OSDAs could not be solved from the room temperature data. To address this challenge, the low-dose cryo-cRED method was used to collect data from as-

made ZMQ-1 at 80 K. The atomic positions of OSDAs were then successfully determined from the difference Fourier map, calculated by comparing the framework model of the as-made ZMQ-1 with the merged low-dose cryo-cRED data. CAU-71-X represents a series of isostructural aluminium(III)-monocarboxylates, where X corresponds to Ac (acetate), Prop (propionate), and TGA (thioglycolate) ligands. Due to the high flexibility of these ligands, their terminal atoms cannot be determined from the room temperature data. To address this, the low-dose cryo-cRED method was employed to stabilize the structures with highly flexible ligands and mitigate the electron-beam damage. This approach not only enabled accurate structure determination but also allowed for the refinement of positional disorder, providing deeper insights into the structural details of the CAU-71 compounds.

2. Background

2.1 Introduction of electron crystallography

Crystals are defined in real space by their long-range ordered atomic arrangements.[25] In reciprocal space, this order is reflected in sharp, well-defined diffraction patterns. Crystallography, as a scientific discipline, focuses on the study of the crystalline structures. By employing diffraction techniques with X-rays[2], neutrons[26], or electrons[8], crystallography enables scientists to uncover the structure of crystals, providing a foundation for understanding and predicting material behavior at the atomic level. Electron crystallography [7], in particular, stands out for its ability to probe micron- or even nano-scale structures with fine details, making it a powerful tool for advancing knowledge of crystalline materials.

2.1.1 Bragg's law

At the core of crystallography lies Bragg's Law [27], a fundamental principle that describes the condition for constructive interference of scattered waves from a crystal lattice (Figure 2.1). Mathematically expressed as:

$$n\lambda = 2dsin\theta \tag{2.1}$$

where d is the interplanar spacing, θ is the angle between the incident beam and the crystal planes, λ is the wavelength of the incident radiation, and n is an integer.

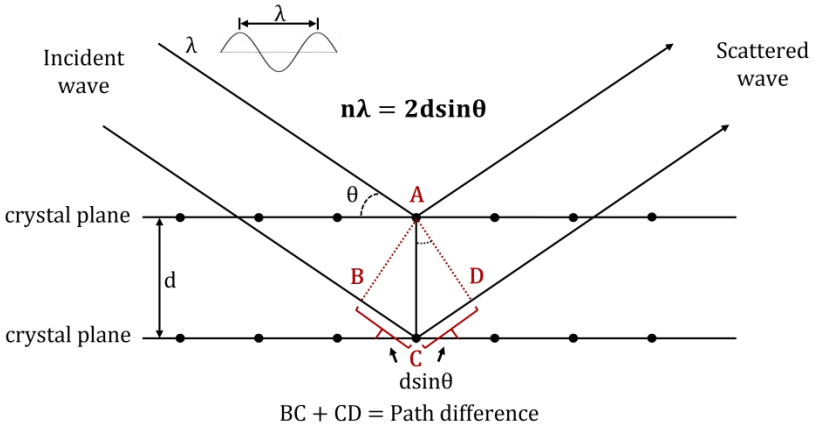

Figure 2.1. Illustration of Bragg's law for constructive interference.

When an incident wave interacts with a crystal, it is scattered by the periodically arranged atoms within the crystal planes. For constructive interference to occur, the path difference between waves scattered by crystal planes must be an integer multiple of the wavelength (nλ). When this condition is satisfied, the scattered waves interfere constructively with each other, generating a bright spot known as a reflection in the diffraction pattern.

In a diffraction pattern, each reflection corresponds to a specific set of crystal planes. The relative positions of reflections are related to the spacing between crystal planes, while the intensities of reflections are determined by the position and types of atoms within the crystal lattice.

2.1.2 The Ewald sphere

In reciprocal space, Bragg's law can be visualized by the construction of the Ewald's sphere (Figure 2.2).[28] This construction involves the reciprocal lattice, which is a mathematical representation of the atomic arrangement in a crystal. Each point in the reciprocal lattice represents a specific set of crystal planes in the real space. The distances between reciprocal lattice points are inversely related to the corresponding interplanar spacing in real space. The key point is that the Bragg condition is satisfied when Ewald's sphere intersects the reciprocal lattice point.

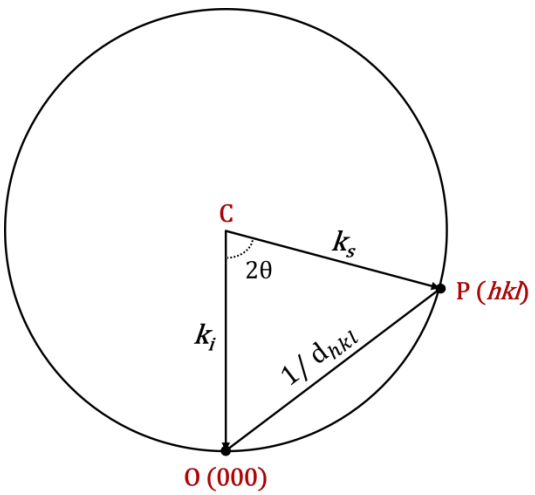

Figure 2.2. The scheme of Ewald sphere.

Ewald sphere is typically represented in two-dimensions by a circle with a radius of the 1/λ. The sphere is centered at the end of the incident wave vector

$\boldsymbol{k_i}$, and the origin of the reciprocal lattice (point **O**) lies at the head of $\boldsymbol{k_i}$. For any reciprocal lattice point (**P**) intersecting the surface of Ewald sphere, the scattered wave vector $\boldsymbol{k_s}$ has the same length 1/λ. The difference between $\boldsymbol{k_i}$ and $\boldsymbol{k_s}$ can be expressed as:

$$|k_i - k_s| = \frac{2\sin\theta}{\lambda} = \frac{1}{d} \tag{2.2}$$

which is the same as Bragg's law in Equation (2.1). This geometric relationship indicates that the set of planes corresponding to point **P** must satisfy the Bragg condition, resulting in a diffraction maximum.[7]

In electron crystallography, the short wavelength of electrons (e.g., 0.0251 Å at 200 kV) results in a significantly larger radius of the Ewald sphere (defined as 1/λ) compared to X-ray diffraction. As a result, the surface of the Ewald sphere in electron diffraction is almost planar in comparison with the array of the reciprocal lattice points (Figure 2.3).

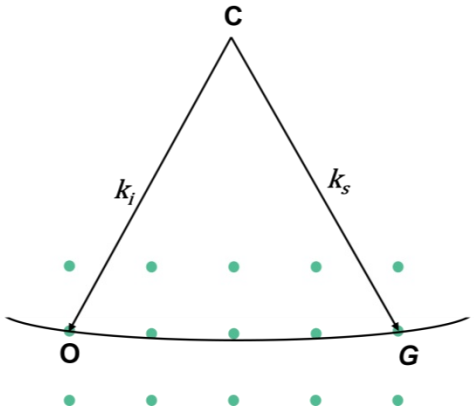

Figure 2.3. The geometry of Ewald's sphere in electron diffraction.

2.1.3 Electrostatic potential and structure factors

Electrons are scattered by the electrostatic potential from atoms in the material. This electrostatic potential can be represented as a continuous three-dimensional function in real space. For a position $r(xyz)$, the electrostatic potential $\varphi(xyz)$ can be expressed as the sum of contributions from all atoms:

$$\varphi(r) = \sum_{j=1}^{N} \varphi_j(r - r_j) \tag{2.3}$$

where:

- r_j is the position of the *j*-th atom in the unit cell.
- The function $\varphi_j(r - r_j)$ represents the potential contributed by the *j*-th atom at position r_j.
- N is the number of atoms in the unit cell.

The electrostatic potential is periodic in the crystal. Therefore, it can be expressed as a summation of Fourier components in reciprocal space, known as structure factors (F) in crystallography. The structure factors are a set of 'waves' with certain amplitudes and phases, which can be represented as discrete points in reciprocal space. Its mathematical expression is:

$$F(hkl) = \sum_{j=1}^{N} f_j(hkl) \mathrm{e}^{2\pi i(hx_j + ky_j + lz_j)} \tag{2.4}$$

where:

- f_j is the electron atomic scattering factor of the *j*-th atom in the unit cell.
- $x_j, y_j \; and \; z_j$ are the fractional coordinates of the atom in the unit cell,
- $h, k \; and \; l$ are the Miller indices of the crystal planes.

In turn, the electrostatic potential $\varphi(xyz)$ in real space can be described by the structure factor $F(hkl)$ in reciprocal space through Fourier transform[29]:

$$FT[\varphi(xyz)] = \frac{h^2}{2\pi me\Omega} F(hkl) = \frac{\lambda}{\sigma\Omega} F(hkl) \tag{2.5}$$

Where h is Planck's constant, m and e are the electron relativistic mass and charge, Ω is the unit cell volume, and σ is the interaction constant.

Therefore, the electrostatic potential $\varphi(xyz)$ can be calculated from the structure factor $F(hkl)$ by in inverse Fourier transform:

$$\varphi(xyz) = \frac{\lambda}{\sigma\Omega} \sum_{hkl} F(hkl) \mathrm{e}^{-2\pi i(hx + ky + lz)} \tag{2.6}$$

Based on Friedel's law $|F(hkl)| = |F(-h - k - l)|$, equation (2.6) can be written as[7]:

$$\varphi(xyz) = \frac{\lambda}{\sigma\Omega}\left[\sum_{hkl}|F(hkl)|\cos[2\pi(hx+ky+lz)-\phi(hkl)]\right] \quad (2.7)$$

Therefore, the electrostatic potential $\varphi(xyz)$ can be described as a summation of cosine waves, each represented with an amplitude $|F(hkl)|$ and a phase $\phi(hkl)$. If the amplitude $|F(hkl)|$ and phase $\phi(hkl)$ can be determined, the electrostatic potential of the structure can be reconstructed. From this potential, the atomic coordinates can be identified, and thus the crystal structure can be solved.

For a reflection (hkl) in a diffraction pattern, its intensity $I(hkl)$ is proportional to the amplitude of structure factor $|F(hkl)|$. This can be expressed as:

$$I(hkl) \propto |F(hkl)|^2 \quad (2.8)$$

However, the phase information is inherently lost in diffraction data. This is known as the *phase problem* in crystallography.

2.1.4 Structure determination by electron diffraction

Structure determination consists of two main steps: structure solution and structure refinement. Due to the *phase problem*, recovering phase information is essential for calculating the electron potential map and determining the initial atomic positions. This process is known as structure solution. Various methods have been developed to recover phase information from diffraction, including Patterson method[30], direct methods[31], and dual-space method[32], all of which have been implemented in software programs such as *SHELX*[33], *PHASER*[34], *SIR*[35,36], and *SUPERFLIP*[37]. In this thesis, *SHELXT*[32], a program within *SHELX* package, was used to solve the structure from 3DED data. *SHELXT* employs dual-space methods, in which the phases of structure factors are retrieved by iteratively modifying the structure factors in reciprocal space and the electron potential in real space. The initial structure model is output once convergence is reached.

While the initial model generated by *SHELXT* is typically of high quality, it may still contain inaccuracies due to limitations of the program-generated phase. Common inaccuracies include: 1) missing atoms; 2) incorrect atom type assignment; 3) inaccurate atomic coordinates; 4) inaccurate occupancy values; 5) inaccurate atomic displacement parameters (ADPs)[38]; 6) missing structural details, such as hydrogen atoms, disorders, and solvent molecules. Better phases can be calculated from the improved structure model, which enables the recalculation of a more accurate electron potential map. By

iteratively refining the phase against the structural model, the differences between calculated and observed diffraction intensities are minimized. This process is called structure refinement. In this thesis, structure refinement was performed by least-squares based SHELXL[39] through the ShelXle interface[40]. The least-squares approach can be described as:

$$M = \sum w \left({F_{obs}}^2 - {F_{cal}}^2 \right)^2 \tag{2.9}$$

where ${F_{obs}}^2$ is the observed intensity, ${F_{cal}}^2$ is calculated intensity from structure model, and w is a weighting factor derived from the standard deviations of the intensities.

The best model is the one that minimizes the value of the minimization function, *M*. The following metrics are used to evaluate the quality of the model obtained from the refinement[41]:

- *R*-factor (R_1): a measure of the discrepancy between the observed structure factor amplitude $|F_{obs}|$ and these calculated from the model $|F_{cal}|$.

$$R_1 = \frac{\sum \left| |F_{obs}| - |F_{cal}| \right|}{\sum |F_{obs}|} \tag{2.10}$$

- Weighted *R*-factor (wR^2): a measure of the discrepancy calculated based on F^2, and takes into account the standard deviations of the intensities (w).

$$wR^2 = \left[\frac{\sum w \left({F_{obs}}^2 - {F_{cal}}^2 \right)}{\sum w \left({F_{obs}}^2 \right)^2} \right]^{1/2} \tag{2.11}$$

- Goodness-of-Fit (GooF): a measure of how well the model fits the observed data, where w is the weighting factor, n is the number of reflections, and p is the number of refined parameters. A value close to 1 suggests a good fit.

$$GooF = \left[\frac{\sum w \left({F_{obs}}^2 - {F_{cal}}^2 \right)}{(n - p)} \right]^{1/2} \tag{2.12}$$

2.2 3D electron diffraction

3DED involves rotating the crystal under an electron beam to collect a sequence of diffraction patterns from different angles. This rotation provides the angular relationship between diffraction patterns, enabling the reconstruction of the 3D reciprocal lattice. Over the years, different 3DED methods have been developed. The earliest method, introduced by Ute Kolb and her group in 2007, is known as automated diffraction tomography (ADT).[42] As shown in Figure 2.4a, ADT involves automated collection of diffraction patterns at a series of discrete tilt angles using the goniometer of a transmission electron microscope (TEM). However, this step-wise mechanical tilting only allowed coarse sampling of the 3D reciprocal lattice, resulting in a large missing wedge. Additionally, the stop-and-start motion between tilts introduced mechanical instability, which complicates the 3D reconstruction.

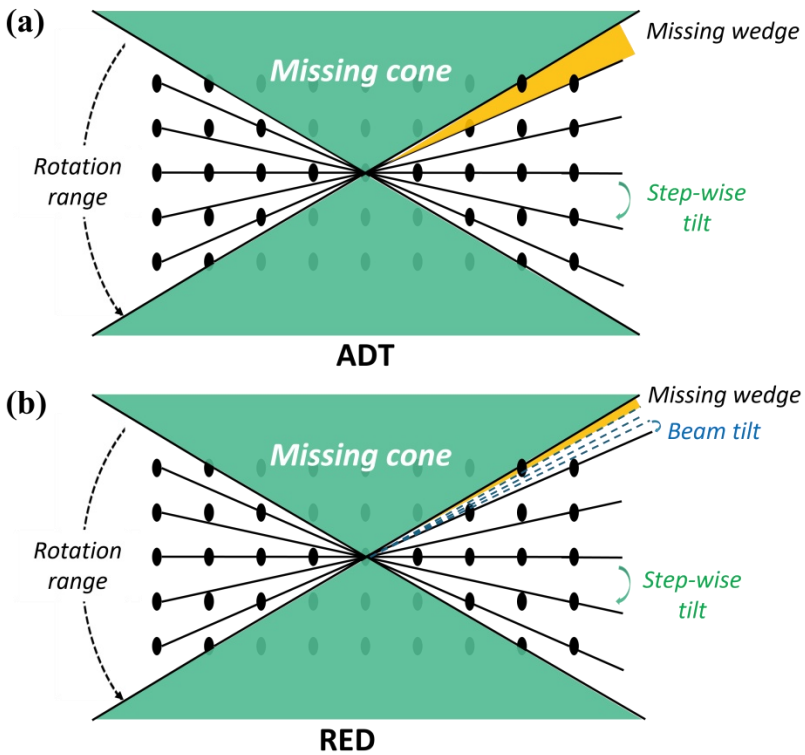

Figure 2.4. The data collection sketches of (a) automated diffraction tomography (ADT) and (b) rotation electron diffraction (RED). *Note: The "missing cone" refers to a region in reciprocal space that cannot be sampled due to the limited tilt range of the goniometer in a TEM.*

To address these challenges, rotation electron diffraction (RED) was developed by Zhang et al. in 2010[43] (Figure 2.4b). RED employs fine beam tilts (e.g., 0.05°) between adjacent mechanical tilts to improve the sampling rate of reciprocal lattice.[44] While this approach partially fills the missing wedge of data through beam tilting, the reconstruction challenges arising from mechanical tilting have not been fully resolved.

The shift toward continuous rotation data collection in 3DED has been driven by the need to minimize beam damage in sensitive materials. This development is enabled by advances in modern detectors with short readout times, such as hybrid pixel detectors and detectors with CMOS (Complementary Metal-Oxide-Semiconductor) technology. In continuous rotation 3DED, the crystal rotates continuously under the electron beam, and diffraction data is acquired through a sequence of frames within minutes (Figure 2.5). Continuous rotation minimizes the missing wedge and mitigates reconstruction issues. Meanwhile, the rapid acquisition process minimizes electron fluence on the sample, making it suitable for highly beam-sensitive materials.

This method has been referred to by various acronyms, including MicroED[45] (Microcrystal Electron Diffraction), IEDT[46] (Integrated Electron Diffraction Tomography), and cRED[47] (continuous Rotation Electron Diffraction). In this thesis, 3DED is used as a general term to encompass all data collected using cRED for simplicity.

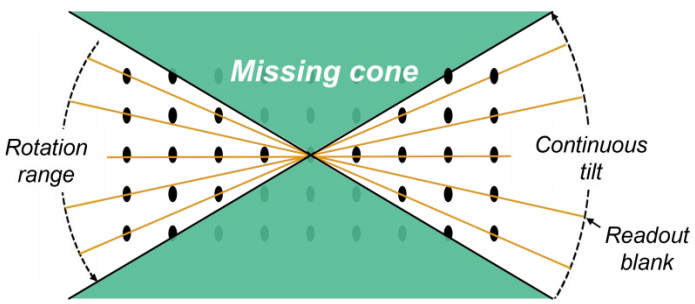

Figure 2.5. The data collection sketches of cRED. *Note: The "missing cone" refers to a region in reciprocal space that cannot be sampled due to the limited tilt range of the goniometer in a TEM.*

2.3 Electron-beam damage

Electron-beam damage is attributed to inelastic scattering, in which incident electrons transfer energy to the specimen during interaction.[20] The

probability of electron-beam damage to a material can be quantified by the cross-section, which measures the probability of specific interactions between electrons and the specimen. There are three primary mechanisms of damage: radiolysis, heating, and knock-on damage (Figure 2.6).[14]

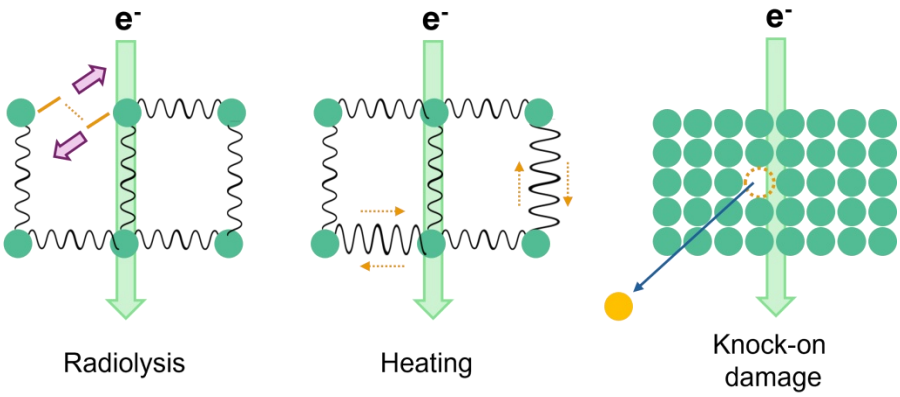

Figure 2.6. Schematic illustration of the mechanisms of radiation damage.

2.3.1 Radiolysis

Radiolysis refers to the structural degradation and chemical change of a specimen due to electron-induced bond dissociation.[14] This process is primarily driven by electron-electron interactions (e.g., ionization), where incident electrons transfer sufficient energy to atomic electrons during inelastic scattering, thereby breaking chemical bonds. The resulting structural degradation leads to a loss of crystallinity, which is observed as a fading of the spots in the diffraction pattern if the specimen is crystalline. Additionally, radiolysis can also cause mass loss through radiolytic decomposition, leading to shrinkage or distortion of the specimen. In the case of organic materials, the cross-section for radiolysis is several orders of magnitude larger than that for knock-on displacement, making radiolysis the dominant damage mechanism even at high accelerating voltages.[48]

The cumulative electron fluence (in $e^-/Å^2$) is critical to manage electron-beam damage.[49] The electron fluence per dataset should be kept below the critical threshold beyond where irreversible damage occurs.

2.3.2 Heating

Heating occurs when the transferred energy enhances atomic vibrations within the specimen, leading to a localized temperature rise.[50] Experimental measurement of heating effects is challenging because many variables can

influence the result, such as the thermal conductivity, thickness, and surface condition of the specimen, as well as the beam size, energy, and current.[20] For materials with high thermal conductivities (k, in W/m·K), such as metals and metalloids (tens to a few hundreds W/m·K), heating is generally negligible in commercial TEM (< 300 kV). However, for materials like polymers and biological tissues, with thermal conductivities typically less than 1 W/m·K, the heating effect must be carefully considered and managed in practice.

One way of alleviating heating effects is cooling the sample to a cryogenic temperature.[51] This is typically achieved using liquid N_2 in cryo-EM (cryogenic electron microscopy) or cryo-holders. Alternatively, reducing the electron flux (in $e^-/Å^2/s$), which refers to the number of electrons passing through a unit area per unit time, can mitigate the heating effect by reducing the rate of heat generation.

2.3.3 Knock-on damage

Knock-on damage occurs when incident electrons displace atoms from their equilibrium positions, creating defects in the specimen. When an incident electron penetrates close to an atomic nucleus, it is decelerated by the Coulombic attraction, thus transferring most of its energy to the atom. If the transferred energy exceeds the threshold energy (E_t) of the specimen, the atomic displacement occurs. E_t is determined by the displacement energy (E_d) and the atomic weight (A) of specific atoms.[20] Compared to bulk atoms, which are tightly bonded in all directions, surface atoms have fewer neighboring atoms. As a result, surface atoms require less energy for displacement. When inelastic scattering occurs at the surface, these atoms can be easily ejected into the vacuum of the microscope. This process is called electron-beam sputtering.[52]

Knock-on damage is directly related to the incident beam energy (E_0, in eV), which is determined by the accelerating voltage (V) applied in TEM. The relationship is expressed as:

$$E_0 = eV \tag{2.13}$$

where e is the elementary charge of an electron (1.602×10^{-19} C), and V is the accelerating voltage in volts. In theory, knock-on damage can be reduced by using low accelerating voltage in a commercial TEM (e.g., 60 keV). However, this approach is not always effective, as lowering the accelerating voltage increases the heating effect and radiolysis. A more practical approach is to reduce the electron fluence to the minimum required for data acquisition.

2.3.4 Challenges for beam sensitive materials

The 3DED analysis of beam-sensitive materials is challenging due to electron-beam damage, which is evident through the fading of diffraction spots during data collection. High-order diffraction spots fade first, as they correspond to smaller atomic spacings.[20] Since beam damage directly affects the spatial resolution of acquired data, mitigating electron-beam damage is crucial for the accurate structural analysis of beam-sensitive materials.

From a materials perspective, beam-sensitive materials can be broadly classified into two categories based on their structures and damage mechanisms: fluence-sensitive and flux-sensitive.[17] Electron fluence (in $e^-/Å^2$) is defined as the total number of incident electrons per unit area. Electron flux (in $e^-/Å^2/s$) is defined as the number of incident electrons per unit area per unit time.

For fluence-sensitive materials, structural degradation is primarily related to cumulative electron fluence. When the total fluence surpasses a defined threshold (i.e., critical fluence), significant electron-beam damage occurs. This behaviour is commonly associated with two damage mechanisms: radiolysis and knock-on damage. A wide range of materials are fluence-sensitive, such as most molecular crystals[53], zeolites[54], and MOFs. While the overall damage effect of fluence-sensitive materials does strongly depend on electron flux, a lower electron flux is still preferred during 3DED data collection as it allows for longer recording times per crystal.

Flux-sensitive materials, on the other hand, exhibit changes in electron-beam sensitivity depending on the electron flux.[17] For materials that become more beam-sensitive with an increased electron flux, a “direct” flux effect is attributed. This effect is related to damage dominated by heating or charging. In these cases, damage may be mitigated when the dose rate is kept below a critical electron flux.

3. Experimental methods

3.1 Sample preparation

3.1.1 General sample preparation for crystalline materials

For 3DED experiments, the suitable crystal size typically ranges from a few hundred nanometers to several micrometers. The most common strategy to prepare 3DED samples is by using mechanical force (Figure 3.1). For most brittle yet robust materials (e.g., inorganic compounds), a mortar and pestle are typically used to crush crystals into small fragments, which are then dispersed in a solvent to form a homogeneous suspension. If necessary, ultrasonication can be used to reduce sample aggregation. A few microliters of the suspension are then deposited onto a TEM grid and air-dried before being loaded into the TEM.

However, strong mechanical forces may damage the crystallinity of certain samples. For fragile samples, such as pharmaceuticals, gentle crushing between two glass slides is preferred to avoid the potential mechanical damage. Additionally, since pharmaceuticals are highly soluble in many solvents, the crushed powder is directly dispersed onto a TEM grid by gently pressing the grid against the crushed powder.

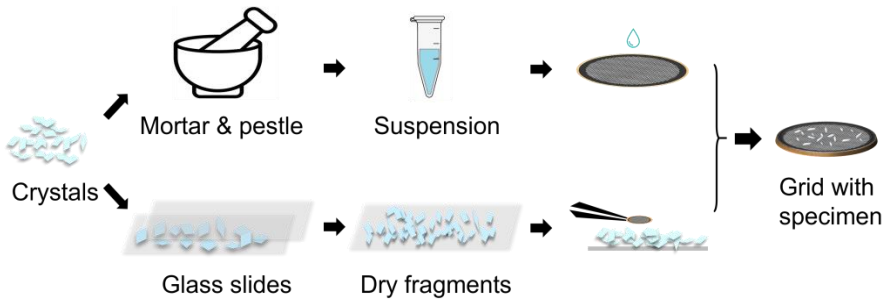

Figure 3.1 Specimen preparation for inorganic and organic materials.

Moreover, a successful grid for 3DED should contain a sufficient number of crystals with proper distribution. This is crucial to ensure adequate sampling while avoiding crystals being too close to each other. It is recommended to check the grid and confirm the sample distribution before setting up the 3DED test, especially when data needs to be collected at cryogenic temperature.

3.1.2 Development of cryo-sample preparation workflow for air-sensitive crystalline materials

In practice, the inherent properties of samples present further challenges for sample preparation. A previous study[55] by Gonen *et al*. reported that certain salt mixtures exhibited a "melted" appearance under TEM, suggesting hydration-induced loss of crystallinity. Similarly, in our study, the beam-sensitive anhydrous sodium valproate was also found to be highly sensitive to moisture. Upon exposure to moisture during sample preparation, the sample exhibited melted-like morphology, with no reflections observed under diffraction mode (Figure 3.2).

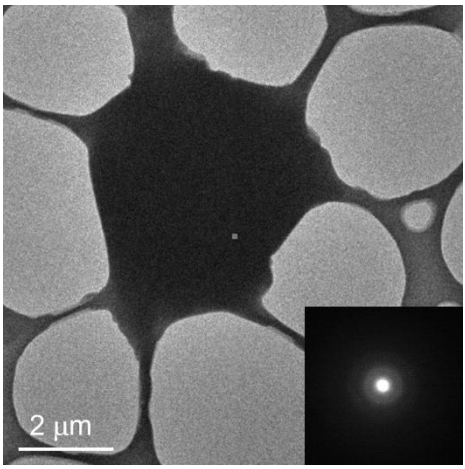

Figure 3.2 The morphology of a "dissolved" anhydrous sodium valproate particle prepared in ambient condition, with corresponding electron diffraction patterns (inset).

Due to the sensitivity of anhydrous sodium valproate to both moisture and electron beam, it was essential to develop a sample preparation method that mitigates these effects.[56,57] To address this, a nitrogen-regulated glovebox equipped with a custom-designed cooling chamber was used to facilitate plunge freezing under a controlled atmosphere. As illustrated in Figure 3.3, the cooling chamber maintains the cryogen after its transfer into the glovebox. A critical challenge in this workflow is preserving the cryogen during transfer through the transfer chamber. This was resolved by transferring ethane in its solid state, rather than its commonly used liquid form, to prevent mass loss under the low-pressure conditions within the transfer chamber.

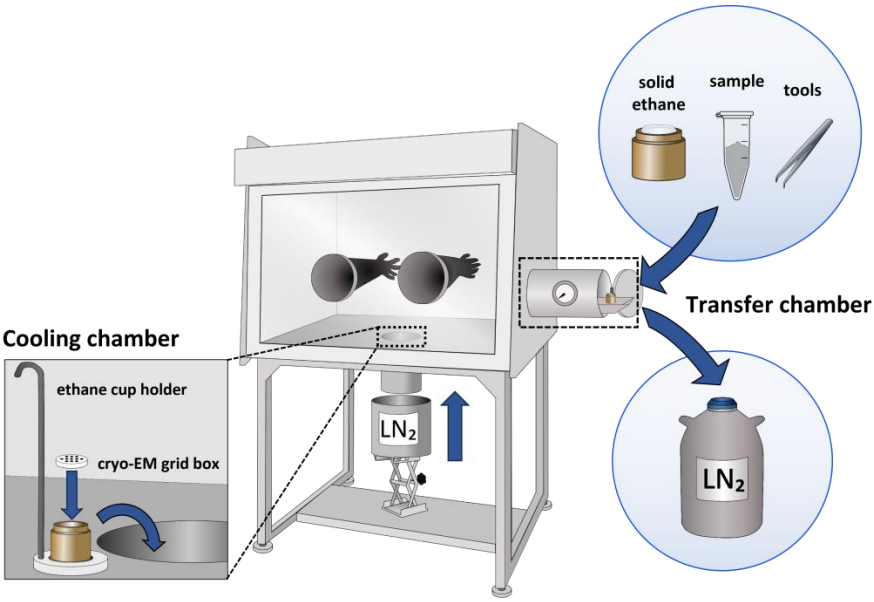

Figure 3.3 Overview of the nitrogen-regulated glovebox with a designed cooling chamber.

The sample preparation workflow was developed with the following steps (Figure 3.4):

Step 1: Solid ethane preparation. Ethane gas is first condensed into liquid in a copper cryogen cup, which is cooled by liquid nitrogen (LN_2). To solidify the liquid ethane, the ethane-filled cup was carefully placed in a bath of LN_2. It is critical to ensure that the cup is surrounded by LN_2, but not fully submerged in the LN_2 bath, which minimizes splashing during the freezing process. Once the ethane solidified, the cup was fully submerged in the LN_2 bath.

Step 2: Glovebox transfer. The solid ethane, along with sodium valproate and essential tools, were transferred into the glovebox via the transfer chamber. Note: Placing tissue beneath the ethane-filled cup can significantly reduce the heat transfer during this process.

Step 3: Specimen preparation.

A cryo-EM grid box is first placed into ethane-filled cup to facilitate following preparation of TEM grids. The cup was then positioned on a 3D-printed ethane cup holder and stored in the cooling chamber when not in use. The crystals were crushed by glass slides and transferred onto TEM grid. These processes were carried out in the glove box.

Step 4: Plunge freeze. The ethane-filled cup was lifted from the cooling chamber, and the as-prepared grid was manually plunged into liquid ethane. The plunge-frozen gird was then placed into a slot of the cryo-EM grid box, which is kept at the bottom of ethane-filled cup.

Step 5: Storage. Once several grids were prepared and stored, the entire ethane-filled cup with the plunge-frozen grids was transferred out of the glovebox and stored in liquid nitrogen for further use.

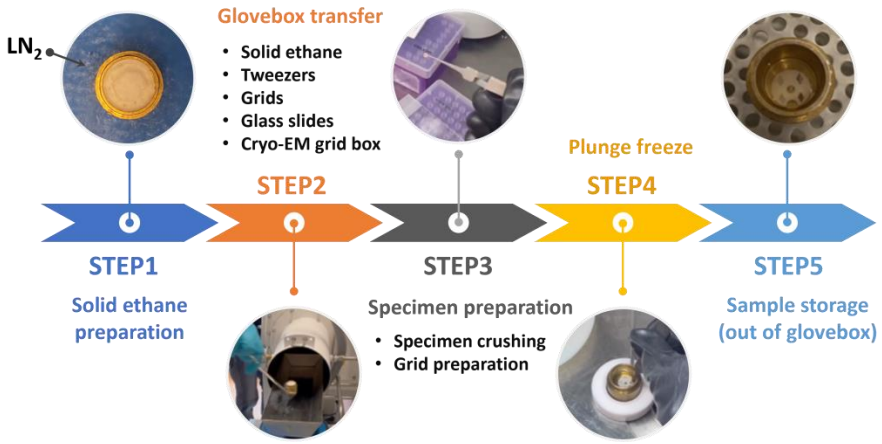

Figure 3.4 The overall workflow of the glovebox-assisted cryo-transfer sample preparation for 3DED.

3.2 Data collection

3DED datasets were collected from isolated crystals with the assistance of data collection software. Before data collection, the specimen must be adjusted to the mechanical eucentric height for further alignment. In diffraction mode, the diffraction spot was focused, and camera length was adjusted to maximize resolution while ensuring efficient detector usage. For crystals within the same grid square, the eucentric height is generally preserved. However, if the sample drifts significantly during rotation, the eucentric height must be realigned.

In this thesis, 3DED experiments performed on JEOL JEM2100-LaB_6. *Instamatic* [58] was used for data collection. During data collection, every *n*-th frames (typically n = 10) was defocused to generate an image in diffraction mode. The crystal position was then corrected by manually adjusting the stage. This crystal-tracking capability effectively compensates for crystal drift during rotation, enabling a wide rotation range for dataset collection (e.g., 120°). For Thermo Fisher Scientific TEMs (Themis Z and Krios G3i), data

were collected using the *EPU-D* software. While the joystick-based control design makes manual crystal adjustment more difficult, the high mechanical stability of their goniometers allows a rotation range of up to 130°, provided the eucentric height is properly set. In this thesis, different microscopes, detectors, holders, and software were used for data collection. A summary of the experimental details of each project is shown in Table 3.1.

Sample	Software	TEM	Detector	Holder	T (K)
Piroxicam	*Instamatic*	LaB_6	Timepix	Single-tilt	293
Sodium valproate	*Instamatic*	Themis Z	One view	Gatan Elsa™ 698	95
Calcined ZMQ-1	*Instamatic*	LaB_6	Timepix	Single-tilt	293
As-made ZMQ-1	*EPU-D*	Krios G3i	CetaD	Autoloader	80
CAU-71-Ac	*Instamatic*	LaB_6	Timepix	Gatan 914	95
CAU-71-Prop	*EPU-D*	Krios G3i	CetaD	Autoloader	80
CAU-71-TGA	*EPU-D*	Krios G3i	CetaD	Autoloader	80

Table 3.1 A summary of experimental setup and conditions for different samples: software, TEM model, detector, holder, and temperature.

3.2.1 Data collection with low electron fluence

For fluence-sensitive samples, the total electron fluence must be optimized to minimize radiation damage while ensuring a signal-to-noise ratio (SNR) typically above 3. Since electron fluence depends on electron flux and recording time, adjusting either parameter effectively reduces the total fluence of a dataset. The electron flux can be reduced by adjusting the condenser aperture and condenser lens (spot size and illumination area), while the recording time can be minimized by modifying the rotation speed (°/s) and rotation range (°). During the data collection of piroxicam (Paper I), the experimental parameters were adjusted to reduce the electron fluence per dataset and minimize the electron-beam damage. The adjusted parameters of each dataset and resulting electron fluence are listed in Table 3.2.

Sample	Dataset number	Spot size	Rotation range (°)	Rotation speed (°/s)	Electron fluence ($e^-/Å^2$)
Form IX	1	3	116	1.17	21.8
	2	3	132	1.17	24.8
	3	3	72	1.17	13.5
	4	5	105	1.17	1.8
	5	3	105	1.17	19.7
Form VIII	1	3	133	1.17	25.0
	2	3	80	0.46	38.3
	3	3	42	0.46	20
	4	3	83	0.46	39.7
	5	3	91	1.17	17.11
	6	1	40	1.17	55.04

Table 3.2 Summary of adjusted experimental parameters and resulting electron fluence for different piroxicam datasets.

In addition to optimizing data collection parameters, another effective approach to reduce the total electron fluence is to avoid irradiating the specimen before data collection. For data collection on JEOL JEM2100-LaB_6, selected-area (SA) aperture was used to select interested specimen under parallel beam. One drawback is that the illuminated area was significantly larger than the specimen. All crystals within the illuminated region were exposed to beam during data collection, not just the interested one. For data collection using SA aperture, it is advisable to move to an unexposed region before acquiring the next dataset to prevent pre-irradiation. In contrast, a micron-sized beam (e.g., 1.5 μm) generated in nanoprobe mode helps preserve surrounding crystals by limiting unnecessary exposure. The Thermo Fisher Scientific TEMs used in this thesis, Themis Z and Krios G3i, both support data collection in nanoprobe mode. In addition to TEM settings, the data collection software can also help minimize the pre-irradiation of samples. When using *EPU-D* (Thermo Fisher Scientific), the scanned Atlas of entire grid allows navigation to the crystal of interest without illuminating it. The *EPU-D* software also features an auto-blank function, which automatically blanks the electron beam when data is not collected. This ensures that the sample is exposed to the electron beam only during data collection, further reducing the total electron fluence during the experiment.

3.2.2 Data collection with cryo-cooling

A complementary approach for reducing electron-beam damage is through cryo-cooling. By cooling the sample to the cryogenic temperature, the structure of crystalline materials can be stabilized and protected against the electron-beam damage during data collection.

For samples that are stable under the high-vacuum environment of TEM (10^{-7} to 10^{-9} Torr), the sample can be inserted into the TEM first at room temperature and then cooled using LN_2. Since the TEM environment is humidity-free, this approach can effectively prevent ice contamination introduced during plunge freezing. However, for vacuum-sensitive samples, plunge freezing is necessary to preserve the structure under high-vacuum environment. In this process, the grid with samples was plunged into cryogen (e.g., liquid ethane) first and then inserted into TEM along with the holder. During the data collection of anhydrous sodium valproate (Paper II), the cryo-cooling was applied to protect the structure from electron-beam damage.

3.2.3 Combining low-dose 3DED with cryo-condition

For highly beam-sensitive materials, combining both strategies is essential to stabilize the crystalline structure and minimize electron-beam damage. In this thesis, this combined approach is referred to as the low-dose cryo-cRED method. A Cryo-TEM (ThermoFisher Scientific Titan Krios G3i) was employed for low-dose data collection due to its high-level automation and ability to minimize pre-irradiation, provided by the *EPU-D* software.

To control the total electron fluence of each dataset, the electron flux was measured before the data collection. After the initial alignment of 3DED, an image of vacuum area was taken to measure the electron flux by the detector readout. The desired electron fluence per dataset can be adjusted for different samples by adjusting experimental parameters. The nanoprobe mode was used to provide parallel beam with a microsize. In the case of OSDAs (Paper III), a flux density of 0.0025 $e^-/Å^2/s$ was used, resulting in a cumulative fluence of 0.375 $e^-/Å^2$ per dataset with a goniometer rotation range of 60°. For CAU-71-X (Paper IV), the electron fluence is 1.06 $e^-/Å^2$ for each dataset.

3.3 Data processing

3DED data processing starts with the reconstruction of 3D reciprocal lattice. This is done using the Rotation ED processing software (RED*p*)[59], which reconstructs the 3D reciprocal lattice from the 2D diffraction frames obtained by 3DED. For a crystal with an unknown structure, the primitive unit cell parameters are first determined from the three reciprocal basis vectors that

can be used to index all reflections in the 3D reciprocal lattice. The primitive unit cell may not always reflect the highest symmetry of the crystal. To account for this, crystallographic computer programs can be used to identify the possible symmetry. In this thesis, the Computational Crystallography Toolbox (*https://cci.lbl.gov/cctbx/lattice_symmetry.html*) was used. In such cases, the primitive unit cell should be transformed into a higher-symmetry unit cell using the suggested transformation matrix. 2D slices of certain reciprocal lattice planes can then be cut from the transformed 3D reciprocal lattice to visualise the reflection conditions for space group determination.

Since the data collection strategy of continuous rotation 3DED is analogous to that of SCXRD, data processing software originally developed for X-ray diffraction can be applied to 3DED datasets. In this thesis, X-ray detector software package (*XDS*)[60] was used to extract reflection information for structure solution. The 3DED dataset is first indexed and integrated using *XDS*, and the result is saved in the file `INTEGRATE.HKL`. The correction step is then performed using the *XDS* program `CORRECT`, which determines the point group, refines the unit-cell parameters, and excludes unreliable reflections. The final result is saved in `XDS_ASCII.HKL` along with a log file containing the processing statistics (`CORRECT.LP`). The resolution cut-off and frame range are modified from the statistics reported in log file, including $I/\sigma(I)$, R_{meas}, completeness, and $CC_{1/2}$. If this step fails, the unit cell and space group obtained from RED*p* can be used for indexing.

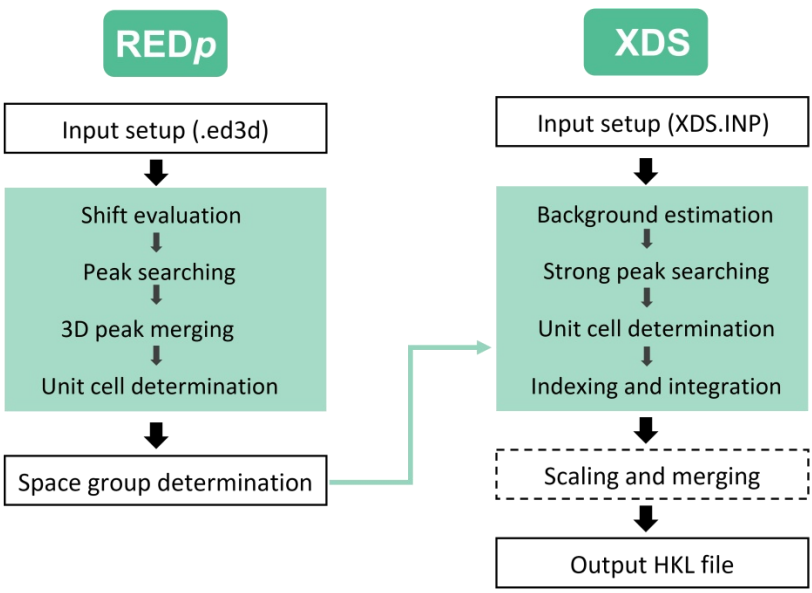

Figure 3.5 The general data processing workflow of 3DED by RED*p* and *XDS*.

Achieving high completeness (above 80%) from a single dataset is often challenging, particularly for beam-sensitive materials. To improve sampling of the reciprocal lattice, multiple datasets are typically collected from different crystals and merged together. Due to mosaicity and/or crystal size, the intensity distribution of diffraction patterns for the same material varies from one to another. To put different reflection files (`XDS_ASCII.HKL`) on a common scale, *XDS* program `XSCALE` is used to scale and merge multiple datasets into a single reflection file. Similarly, a log file (`XSCALE.LP`) is generated to evaluate the merging statistics, including $I/\sigma(I)$, R_{meas}, completeness, redundancy, $CC_{1/2}$, and pairwise cross-correlation of datasets. The general data processing workflow is demonstrated in Figure 3.5.

Besides improved completeness, the enhanced redundancy of merged data also contributes to the quality of structure model. Redundancy is defined as the ratio of the total number of measured reflections to the number of unique reflections, as shown in the following equation:

$$\text{Redundancy} = \frac{\text{Total number of measured reflections}}{\text{Number of unique reflections}} \tag{3.1}$$

A high redundancy means that the same diffraction reflection (unique reflection) is measured multiple times. By averaging these repeated measurements, random errors are reduced, bringing the measured intensities closer to their true values. Therefore, using merged data for structure solution is highly recommended. However, manually merging datasets can be time-consuming and laborious, as it involves extensive data processing and classification. To improve efficiency, automated batch processing is highly desired.

In 2024, An XDS-based Graphical User Interface for Automated Real-time and Offline Batch 3D ED/MicroED Data Processing (AutoLEI) was developed in Zou's group. This tool leverages the data processing capability of *XDS* and enables both offline and real-time batch data processing. As shown in Figure 3.6, AutoLEI automates the execution of *XDS* on the input datasets and processes the output files generated by *XDS*. It lists the primitive unit cells of all indexable datasets and suggests possible space groups for each unit cell through `Estimate Symmetry`. Based on the suggested space group and unit cell parameters, the selected datasets are re-indexed accordingly. `XDSrefine` is then performed to improve data quality by refining or adjusting input parameters. After this, the processed dataset are classified into different clusters based on pair-wise correlation coefficients of reflection intensities, which are reported in "`XSCALE.LP`". These datasets are then merged into a single reflection file for further structure solution. Except for

the data of anhydrous sodium valproate, the data processing for the other three projects was carried out using the offline data processing function of AutoLEI.

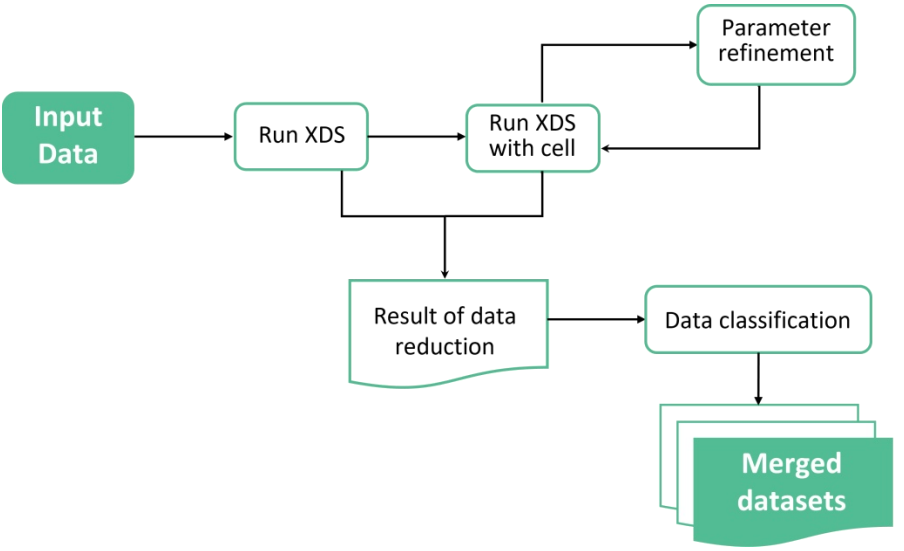

Figure 3.6 The offline data processing workflow of AutoLEI.

3.4 Structure determination

3.4.1 Structure solution

For structure solution in this thesis, the program *SHELXT* was used exclusively. Therefore, the obtained reflection file was first converted into *SHELX* format using the *XDS* program `XDSCONV`. After this, the *SHEXTL*[61] program `XPREP` was used to examine the space group, and generate an input file for structure solution.

3.4.2 Structure refinement

The structure refinement was carried out using the program *SHELXL*. The refinement process began by updating the input file with the electron atomic scattering factors and wavelength of electron beam. Initially, isotropic refinement was performed through several rounds until the result converged. A common criterion for convergence is the `Max Shift` value, which indicates the maximum displacement of atoms between two consecutive refinement cycles. Once Max Shift = 0.000, the refinement was considered converged.

To finalize the structure, any missing atoms were identified and added based on Q-peaks, and the elements of atoms were assigned based on chemical information. Additional rounds of isotropic refinement were then carried out until convergence was achieved again. In this stage, the ADPs were treated as a single value for each atom, assuming that atoms move uniformly in all directions.

Subsequently, anisotropic refinement was carried out, where the ADPs were refined independently along six directions. This step allows for a more accurate description of atomic vibrations. In some cases, the occupancies of certain atoms were also refined, especially in the presence of positional disorder.

Once the anisotropic refinement converged, hydrogen atoms were added to the model. The geometry of the structure was then checked, and restraints were applied if necessary to ensure bond lengths, angles, and other geometrical parameters. Finally, the model was validated using the `checkCIF` program[62] to ensure the model met expected standards of crystallographic analysis.

3.4.3 Positional disorder refinement

In cases where positional disorder was present, additional refinement steps were required. Positional disorder arises when one atom occupies multiple sites.[41,63] This can occur within a single unit cell (dynamic disorder), where the atom undergoes real motion in the solid state; or it can be distributed among different unit cells (static disorder). Despite their different origins, both types of positional disorder are treated in the same way during refinement.

To accurately model positional disorder, each disordered position must be defined, along with its corresponding occupancy. In *SHELXL*, the position of a disordered atom is split into multiple sites, based on the suggested coordination from the program. These split atoms are called equivalent atoms. To avoid equivalent atoms being bonded together, the `PART number` instruction is used to assign them into different groups. The number of `PART` defines disorder groups, ensuring that only atoms within the same group can form bonds.

For general positional disorder, where an atom occupies two alternative positions, `PART 1` and `PART 2` are used. To maintain a chemically meaningful model, the sum of the occupancies of equivalent atoms must equal 1. This rule is enforced by introducing a free variable in the `FVAR` line, following the overall scale factor (*osf*). Correspondingly, the site occupancy factors (*sof*) value of the disordered atoms are changed from 11.00 to 21.00 for atoms in `PART 1` and −21.00 for these in `PART 2`. The ‘2’ in ± 21 links

the occupancies of equivalent atoms to the second free variable in the FVAR line, while the '±' ensures that their total occupancy remains 1. The value of the second free variable represents the occupancy of atoms assigned *sof* of 21.00. An example is provided in Figure 3.7:

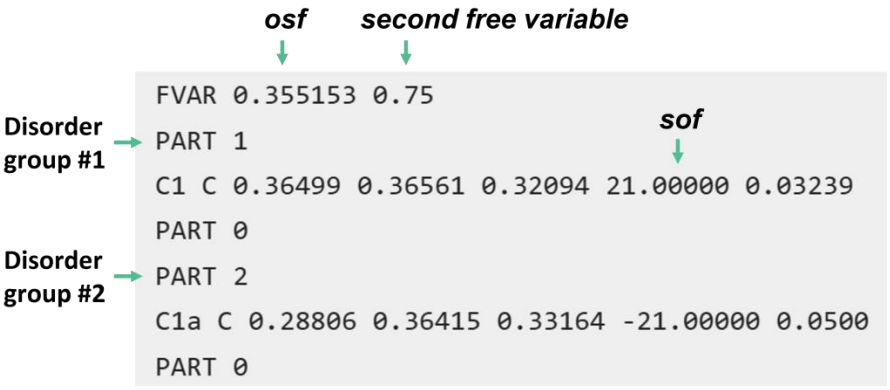

Figure 3.7. An example of positional disorder refinement.

For cases involving more than two disordered components, the SUMP command is used to enforce that the total occupancy equals 1. For instance, if one atom occupies three disordered positions (A1, A2, A3), the SUMP instruction ensures that their occupancies sum to 1 by refining the corresponding free variables (var1, var2, and var3). The command:

```
SUMP 1 0.01 1 var1 1 var2 1 var3
```

ensures that:

$$1 \pm 0.01 = 1*\text{occ(A1)} + 1*\text{occ(A2)} + 1*\text{occ(A3)}.$$

For the three-component disorder in CAU-71-TGA, the SUMP instruction was written as SUMP 1 0.01 1 3 1 4 1 5. The values 3, 4, and 5 refer to the third, fourth, and fifth free variables in the FVAR line, which were assigned to three equivalent atoms on the thiol group.

4. Structural studies of pharmaceuticals

The structures of pharmaceutical compounds strongly influence their physicochemical properties. Even minor structural differences can lead to significant changes in behavior. A key example of this is polymorphism[64], which refers to the ability of a molecule to crystallize into multiple distinct structures. Polymorphism arises from differences in molecular conformation[65], intermolecular interactions and crystal packing. These differences give rise to polymorphs[66], each representing a unique solid-state form of the same molecule. Different polymorphs can exhibit significant differences in solubility and dissolution rates, which directly influence bioavailability. Moreover, polymorphs often differ in physical stability, which is crucial for the formulation and long-term storage of pharmaceutical products. During storage, a polymorph may transform into a more stable form, potentially impairing its therapeutic performance in clinical practice.

Due to these critical implications, extensive efforts in both industry and research have been dedicated to the discovery of pharmaceutical polymorphs.[67,68] In recent years, melt crystallization[69–71] has gained increasing popularity for polymorph discovery, as it can access crystal forms that are often inaccessible through solution crystallization.[72] However, this technique frequently yields nano- to microcrystalline products with limited quantity and occasional multiphases, which complicates structural analysis using traditional X-ray diffraction.[13,73] To overcome these limitations, 3DED offers a promising solution for the structural analysis of polymorphs.[13,47] In this chapter, we present the structure studies of two pharmaceuticals, piroxicam (PXM) and anhydrous sodium valproate, demonstrating the effectiveness of 3DED in uncovering their polymorphic forms.

4.1 Structure studies of piroxicam (PXM) polymorphism

Piroxicam (PXM), a nonsteroidal anti-inflammatory drug (NSAID), is commonly used to alleviate symptoms of arthritis (Figure 4.1). Due to its complex molecular conformation, PXM exhibits rich polymorphism. Over the past 40 years, it has been the focus of extensive research in polymorph discovery. Up to now, seven polymorphs with known structures have been identified, including forms I (β), α1, II (α2), III, IV, VI, and VII. The structures of the first three PXM polymorphs were determined by X-ray diffraction shortly after their discovery.[74–76] In 1985, melt crystallization was introduced into the synthesis process, and facilitated the discovery of form III and IV.[77] However, both structures remained unsolved until 2016, when high-quality

crystals were obtained for X-ray diffraction.[78] In 2020, forms VI and VII were discovered using a melt microdroplet method and later solved by SCXRD.[79]

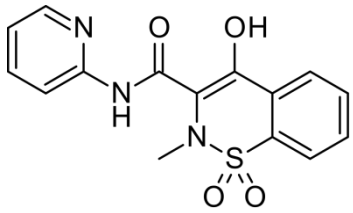

Figure 4.1 The molecular structure of piroxicam.

More recently, in 2023, Yao *et al*. synthesized two new polymorphs through melt crystallization, forms VIII and IX. As shown in Figure 4.2, these polymorphs were identified based on their distinct melting points and Raman spectra, which differentiated them from previously reported forms. However, due to their limited crystal size, their structures remained unsolved by X-ray diffraction. To overcome the limitation of crystal size, we used 3DED for the structure determination of form VIII and IX. Both forms exhibited beam sensitivity during data collection, necessitating the use of low electron fluence to mitigate the electron-beam damage. Under this condition, the diffraction resolution was extended to 0.9 Å for form VIII and 1 Å for form IX, enabling successful structural determination of both forms.

The newly solved structures provide insight into the complexity of PXM polymorphism. By comparison with reported form IV, the structure of form VIII offers a detailed understanding of the structure-property relationship between intermolecular hydrogen bonding and the melting point.

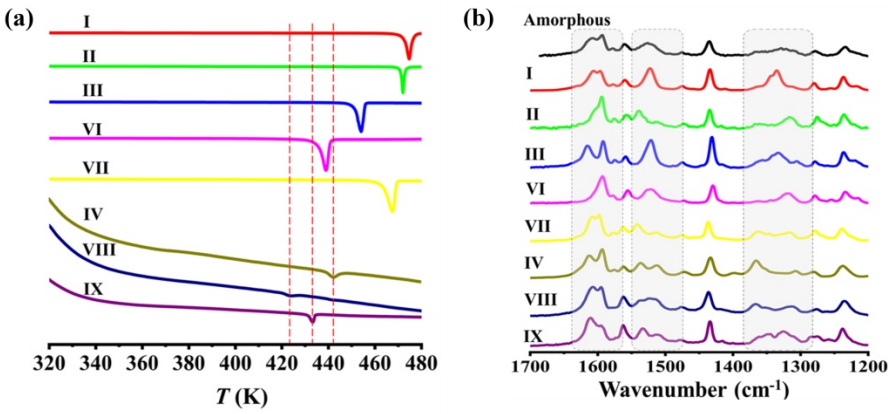

Figure 4.2 (a) Melting points of piroxicam polymorphs. (b) Raman spectra of piroxicam polymorphs. The figure is reproduced from Xu *et al*. with the permission of ACS Publications.

4.1.1 Structures of PXM Form VIII and IX.

Form VIII crystallized in triclinic space group *P*1 (No.1) and contained five independent molecules with distinct molecular conformations in the asymmetric unit (Table 4.1). As shown in Figure 4.3(a-b), Mol.1 and Mol.2, as well as Mol.3 and Mol.4, each form a piroxicam dimer via N−H···N intermolecular hydrogen bonds between the amide N−H and the pyridine nitrogen atoms. Mol.5 is stabilized within the asymmetric unit by van der Waals force.

Form IX crystallized in space group $P2_1/n$ (No.14) and consisted of two independent molecules in the asymmetric unit, as shown in Figure 4.3(c-d). These two PXM molecules, which have similar conformation, form a dimer via N−H···N intermolecular hydrogen bonds between the amide N−H and the pyridine nitrogen atoms.

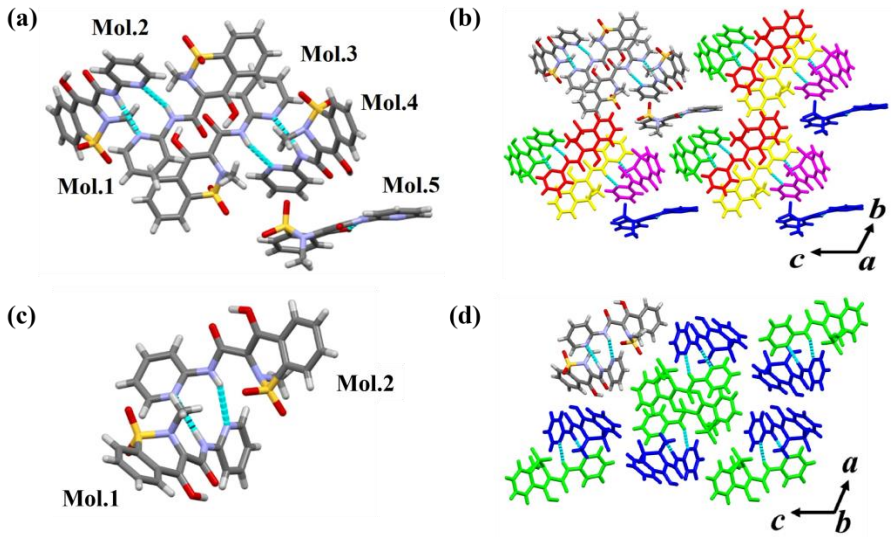

Figure 4.3 (a-b) The asymmetric unit of form VIII and the corresponding crystal packing viewed along *a*-axis. (c-d) The asymmetric unit of form IX and the corresponding crystal packing viewed along *b*-axis. The independent molecules present in the asymmetric unit are labeled as Mol. X (where X corresponds to the molecule number). The figure is reproduced from Xu *et al*. with the permission of ACS Publications.

4.1.2 Relationship between melting point and hydrogen bonding

The form VIII of PXM shares a highly similar crystal packing with the reported form IV, yet their melting points are significantly different. As shown in Figure 4.2, the form VIII exhibits a melting point at 420 K, while the reported melting point of form IV is 439 K. This indicates a noticeable

difference of 19K despite their similar crystal packing, which is presumably attributed to differences in intermolecular interactions. As shown in Figure 4.4, the key distinction lies in the intermolecular hydrogen bonding between different Mol.5s. In form IV, adjacent Mol.5s are linked through N–H···O intermolecular hydrogen bonds via the amide N–H and the acyl group oxygen atoms. In contrast, adjacent Mol.5s in form VIII lack such intermolecular hydrogen bonding. As a result, the intermolecular interactions in form VIII are weaker than in form IV.

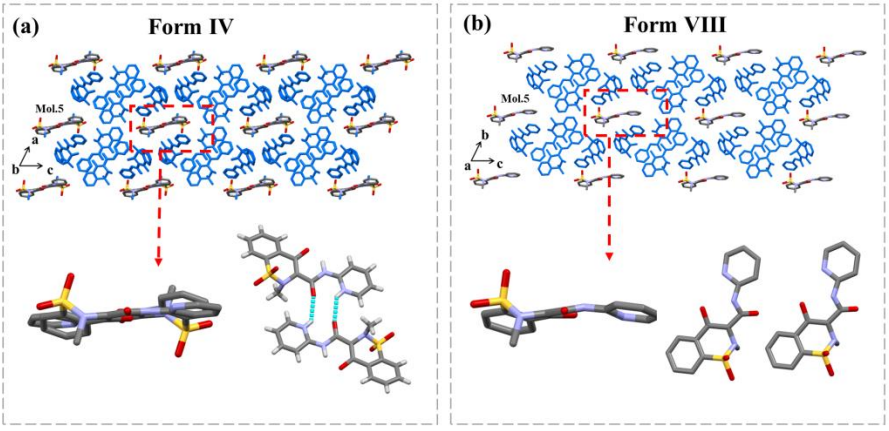

Figure 4.4. Crystal packing of form IV is viewed along *a*-axis (a) and form VIII (b) viewed along *b*-axis. The only difference (Mol. 5) was labelled by red box. The figure is reproduced from Xu *et al*. with the permission of ACS Publications.

Table 4.1 The crystallographic data of PXM form VIII and IX.

Sample	PXM_VIII	PXM_IX
Crystal system	Triclinic	Monoclinic
Space Group	$P1$	$P2_1/n$
a (Å)	13.09(3)	19.71(4)
b (Å)	7.52(15)	7.97(16)
c (Å)	20.84(4)	21.37(4)
α (°)	84.64(3)	90
β (°)	75.44(3)	105.93(3)
γ (°)	84.28(3)	90
Volume	1970.6(7)	3228.0(12)
Z	4	8
Wavelength (Å)	0.02508	0.02508
Radiation type	Electron	Electron
Temperature (K)	293(2)	293(2)
Completeness (%)	89.3	94.0
No. of reflections (all unique)	10607	3168
No. of reflections (Fo>4σ(Fo))	18923	34999
Refined parameters	405	398
R_{int}	0.2136	0.3094
R_1 (Fo>2σ(Fo))	0.2211	0.1633
R_1 (all reflections)	0.2945	0.1991
GOF	0.955	1.044

4.2 Structure studies of anhydrous sodium valproate

Sodium valproate, a widely used antiepileptic drug, has shown significant efficacy in treating various types of seizures and epileptic disorders.[80,81] In contrast to its original form, valproic acid, sodium valproate features the replacement of the carboxyl proton (–COOH) with a sodium ion (Na^+). This ionization enhances its hydrophilicity and improves its solubility.[82] To gain deeper insights into its physicochemical properties, it is essential to determine the crystal structure of anhydrous sodium valproate. However, the enhanced hydrophilicity makes it prone to deliquescence in humid environment. As shown in Figure 4.5, anhydrous sodium valproate deliquesced when exposed to a relative humidity (RH) above 40%, making sample preparation under ambient conditions challenging. Combined with its beam sensitivity, a solution must be found to achieve plunge freezing in a humidity-free environment.

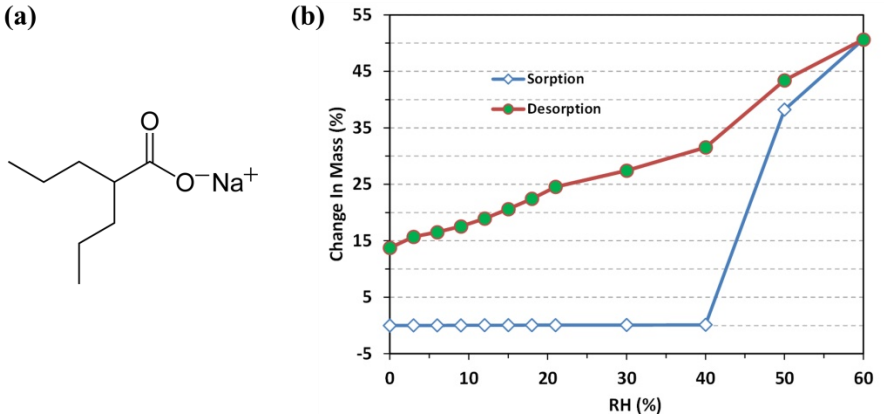

Figure 4.5. (a) The chemical formula of sodium valproate. (b) Moisture sorption isotherm of sodium valproate at 298 K. The sudden rise in mass at > 40% RH indicates deliquescence of sodium valproate. The figure is reproduced from Paper II (ChemRxiv. 2025; doi:10.26434/chemrxiv-2025-8qxqp).

To overcome these challenges, we developed a glovebox-assisted cryo-sample preparation workflow inspired by the glovebox designed by Högbom's group (Department of Biochemistry and Biophysics, Stockholm University). By transferring solid ethane into the glovebox, we enabled plunge freezing within a controlled, humidity-free atmosphere. The detailed steps of this process are presented in Section 3.2.1. Using this workflow, we successfully prepared plunge frozen grids of anhydrous sodium valproate with preserved crystallinity (Figure 4.6a). Based on the 3DED data collected from these

crystals, we were able to solve the structure of the first anhydrous sodium valproate. The workflow can also be used for the sample preparation of air-sensitive materials, such as battery materials and biological samples.

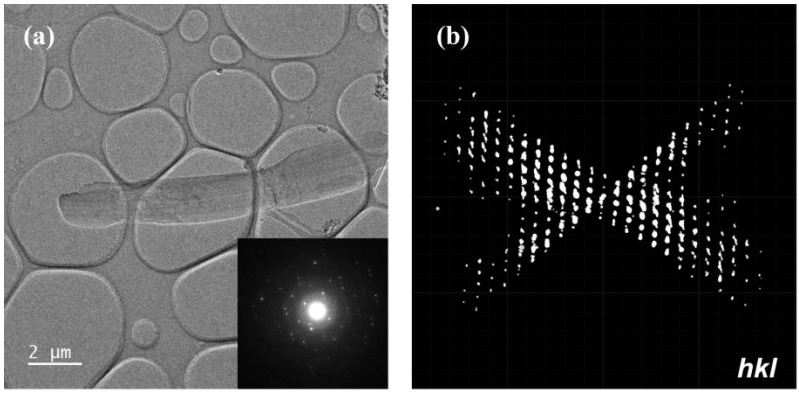

Figure 4.6 (a) TEM bright-field (BF) images of anhydrous sodium valproate prepared within the glovebox. (c) Reconstructed 3D reciprocal lattice of anhydrous sodium valproate. The figure is reproduced from Paper II (*ChemRxiv. 2025*).

4.2.1 Structure of anhydrous sodium valproate

The structure of anhydrous sodium valproate was solved in the monoclinic space group *Cc* (No. 9) (Table 4.2). As shown in Figure 4.7, anhydrous sodium valproate adopts a formulation of $Na_3(valp)_3$ [valp = valproate] within the asymmetric unit. These three sodium cations coordinate with carboxylate groups ($–COO^–$) through oxygen atoms, forming a one-dimensional coordinated chain along *c*-axis.

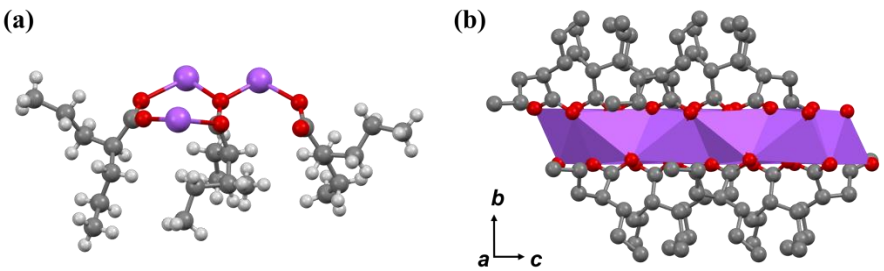

Figure 4.7 Structural model of sodium valproate. (a) Asymmetric unit of sodium valproate. Color code: purple, sodium; red, oxygen; grey, carbon; light grey, hydrogen. (b) Fragment of the crystal packing of sodium valproate viewed along *a*-axis with sodium cations presented in polyhedral form. The figure is reproduced from Paper II (*ChemRxiv. 2025; doi:10.26434/chemrxiv-2025-8qxqp*).

The distorted geometry around sodium cations is a noteworthy feature of the structure. As shown in Figure 4.8a, Na1 is six-coordinated, adopting a slightly distorted trigonal prism geometry. The other two (Na2, Na3) are five-coordinated, each exhibiting a distorted square pyramidal geometry. All of these coordinations exhibit distortion from their standard geometry, resulting in a flexible environment around the sodium ions (Figure 4.8b). The crystal packing of anhydrous sodium valproate is shown in Figure 4.8c. The alkyl chains of valproates surround the sodium ion clusters and interact with each other through van der Waals forces. These structure details of anhydrous sodium valproate provide valuable insight into its hygroscopicity and deliquescence behavior.

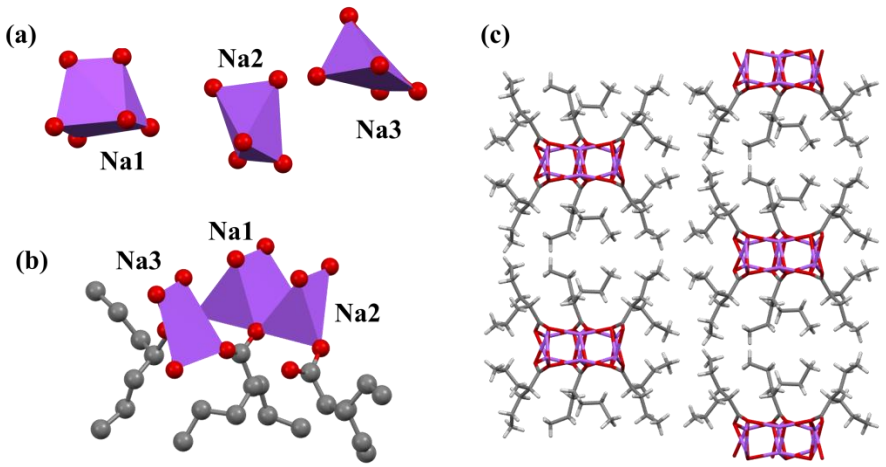

Figure 4.8 (a) Coordination environments of sodium cations in sodium valproate. (b) Coordination mode of sodium cations with valproate ions in sodium valproate. (c) Crystal packing of sodium valproate along the c-axis. Color code: purple, sodium; red, oxygen; grey, carbon; light grey, hydrogen. The figure is reproduced from Paper II (*ChemRxiv. 2025; doi:10.26434/chemrxiv-2025-8qxqp*).

4.2.2 Monohydrate and anhydrous sodium valproate

The structure of anhydrous sodium valproate also provides insight into its polymorphism. The monohydrate form[83] crystallized in the triclinic space group *P*-1, with a water molecule coordinating to the sodium ion. The crystal packing of monohydrate sodium valproate is shown in Figure 4.9a. Similar to the anhydrous form, the monohydrate form is stabilized by van der Waals interactions between the alkyl chains of valproates. The sodium-oxygen coordination clusters of monohydrate form and anhydrous form are shown in Figures 4.9b and 4.9c, respectively. The anhydrous form exhibits a more

compact and orderly atomic arrangement than that of the monohydrate form. The calculated density of the anhydrous form is 1.195 g/cm^3, whereas the monohydrate form has a lower density of 1.099 g/cm^3.

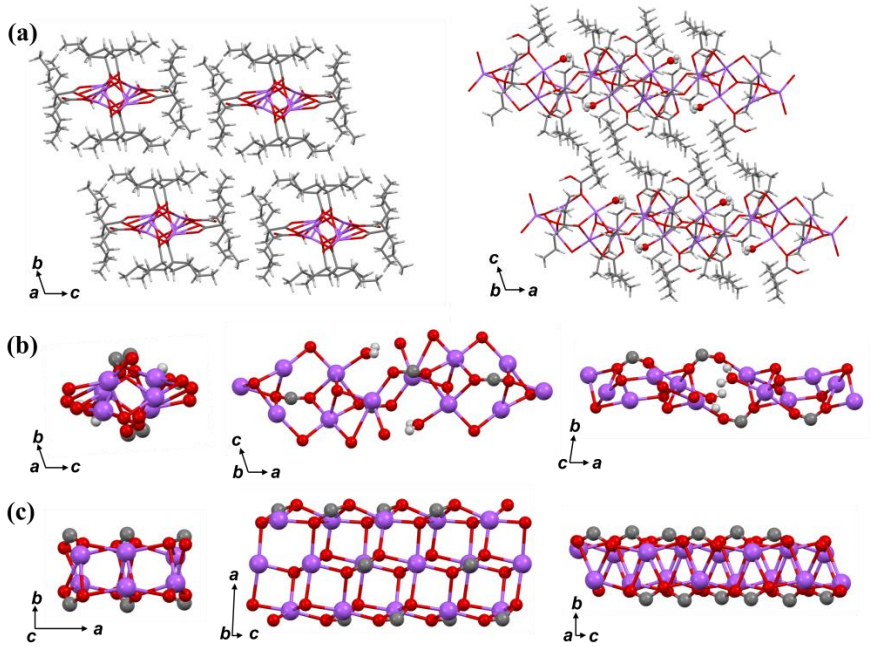

Figure 4.9 (a) Crystal packing of monohydrate sodium valproate along the *a*-axis and *b*-axis. Color code: purple, sodium; red, oxygen; grey, carbon; light grey, hydrogen. (b) 3D structure of the sodium–oxygen clusters in monohydrate sodium valproate along the *a*-, *b*-, and *c*-axis. (c) 3D structure of the sodium–oxygen clusters in anhydrous sodium valproate along *c*-, *a*-, and *b*-axis. The figure is reproduced from Paper II (*ChemRxiv. 2025; doi:10.26434/chemrxiv-2025-8qxqp*).

Table 4.2 The crystallographic data of anhydrous sodium valproate.

Sample	Anhydrous sodium valproate
Crystal system	Monoclinic
Space Group	*Cc* (No. 9)
a (Å)	31.06(6)
b (Å)	14.36(3)
c (Å)	6.24(1)
β (°)	95.28(3)
Volume	2771.96
Z	4
Wavelength (Å)	0.01968
Radiation type	Electron
Temperature (K)	95(2)
Completeness (%)	87.1
No. of reflections (all unique)	4690
No. of reflections (Fo>4σ(Fo))	2038
Refined parameters	139
R_{int}	0.2690
R_1 (Fo>2σ(Fo))	0.2409
R_1 (all reflections)	0.3256
GOF	0.983

5. Structural studies of porous materials

Porous materials [84] are a diverse class of functional materials characterized by the presence of pores within their structures. Based on pore size, they can be classified into three categories: microporous (< 2 nm), mesoporous (2–50 nm), and macroporous (> 50 nm).[85] In addition to size-based classification, porous materials can also be distinguished by their composition and structural nature, ranging from inorganic materials to bio-based materials. This broad range includes materials such as zeolites[86], metal-organic frameworks (MOFs)[87], covalent organic frameworks (COFs)[88], hydrogen-bonded organic frameworks (HOFs)[89], and porous hydrogels[90].

Porous materials have gained significant attention due to their unique structural characteristics, such as high surface area, tunable pore size, and chemical versatility.[91] These features enable their use in various fields, including catalysis, gas storage and separation, drug delivery, water purification and energy storage.[92] Researchers are actively exploring and developing novel porous materials to enhance their performance and expand their potential applications.[93,94]

Structure determination of porous materials plays a crucial role in understanding their properties, synthesis mechanism, and performance. In recent years, 3DED has become a powerful technique for determining the structures of crystalline porous materials.[95,96] In this thesis, two kinds of porous materials were studied using 3DED: zeolite and MOFs.

5.1 Structure studies of the first meso-microporous zeolite ZMQ-1

Zeolites are a class of crystalline porous aluminosilicates, composed of corner-sharing tetrahedra TO_4 (where T = Si, Al, etc.).[97,98] The tetrahedral atoms (T-atoms) are interconnected via oxygen bridges, forming well-defined pores and channels. Over the past century, microporous zeolites have revolutionized the fine chemical and petroleum industries through their size/shape-selectivity for adsorption/separations and catalysis. However, the small size of micropores hinders their application in processing bulky molecules. To overcome this challenge, significant efforts have been dedicated to the synthesis of mesoporous zeolite. Although some success[99,100] has been achieved by incorporating germanium (Ge) into silica framework, the resulting germanosilicate zeolites often suffer from poor stability after the removal of OSDAs, which hinders their practical applications. Therefore, the

challenge of synthesizing stable zeolite with intrinsic mesoporous channel remained unsolved until the breakthrough presented in this section.

In this study, a bolaform phosphonium-based OSDA (denoted as Tri-Cy-dC8) was used for the synthesis of mesoporous zeolite.[101–103] As shown in Figure 5.1, Tri-Cy-dC8 contains an octamethylene chain with a positively charged phosphorus (P) atom at each end. Each P atom is bonded to three cyclohexyl groups, forming a tricyclohexylphosphium structure. The synthesized zeolite was denoted as ZMQ-1 (Zeolitic Materials, Qingdao Institute of Bioenergy and Bioprocess Technology, No. 1).

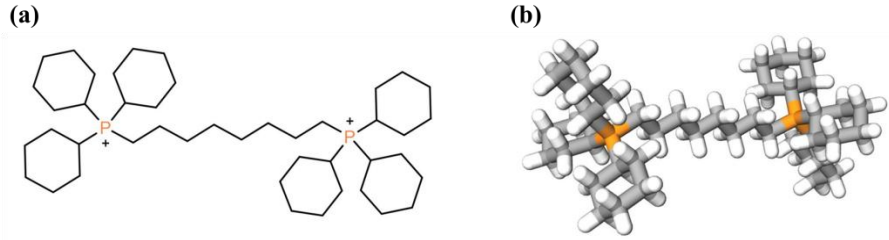

Figure. 5.1 The 2D (a) and 3D (b) structure of the OSDA. The figure is reproduced from Lu *et al*. with permission from Springer Nature.

To evaluate its porosity, Argon adsorption-desorption isotherms were performed at 87K. As shown in Figure 5.2b, the pore size distribution suggests the presence of ~2 nm pores, potentially within the mesoporous range (2-50 nm). However, precise structural determination is necessary to confirm the exact pore dimensions.

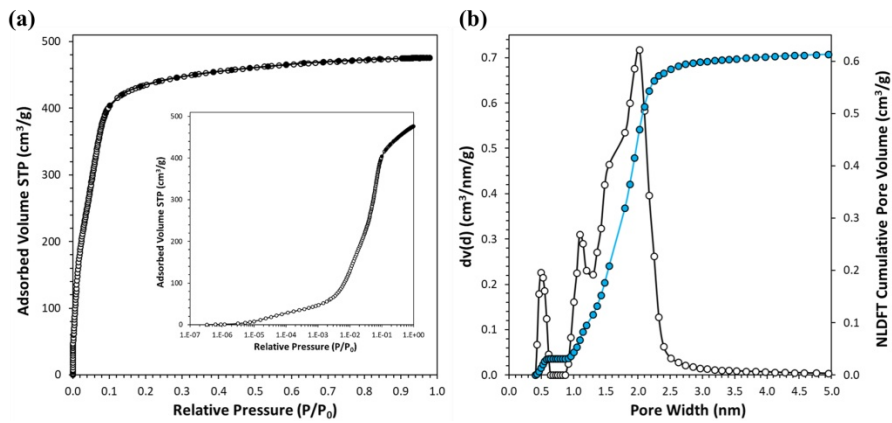

Figure. 5.2 (a) Ar adsorption-desorption isotherm of the ZMQ-1 zeolite and (b) corresponding cumulative pore volume plot and pore size distribution. The figure is reproduced from Lu *et al*. with permission from Springer Nature.

Furthermore, distinct differences between the PXRD patterns (Figure. 5.3) of calcined and as-made ZMQ-1 underscore the importance of structural analysis to understand the detailed atomic rearrangement.

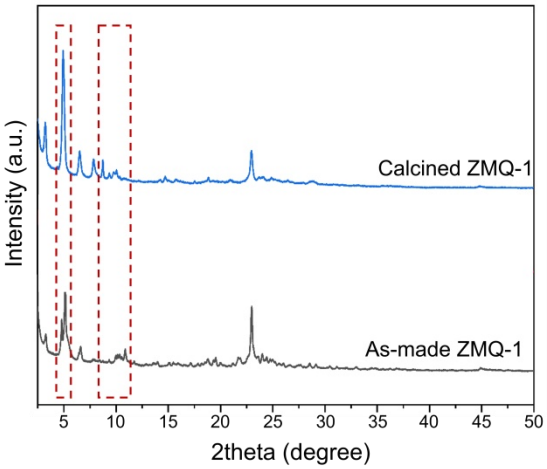

Figure. 5.3 The PXRD of calcined and as-made ZMQ-1.

ZMQ-1 samples were crystallized in nano-sized products, therefore, 3DED was employed for the structural analysis. Both as-made and calcined samples exhibit low beam sensitivity; thus, the 3DED datasets were first collected at room temperature. The solved structures revealed a unique meso-microporous channel system within ZMQ-1, which is delimited by 28 × 10 × 10-rings. The 28-ring has a free diameter of 22.76 Å × 11.83 Å, which makes ZMQ-1 the first stable mesoporous zeolite with intrinsic 3D channel.

Furthermore, the observed structural rearrangement between the calcined and as-made samples explained the differences in their PXRD patterns. To explore the underlying mechanism, we determined the atomic positions of OSDA. Even though the ZMQ-1 framework showed good stability under the electron beam, the OSDAs were vulnerable to the electron-beam damage. To address this challenge, we used low-dose cryo-cRED method to collect data from as-made ZMQ-1. The atomic positions of OSDAs were then determined by the structure refinement against the low-dose cryo-cRED data, using the framework solved from room temperature data.

5.1.1 Structures of as-made and calcined ZMQ-1

The as-made ZMQ-1 crystallized in the monoclinic space group *P*2/*m* (No. 10), whereas the calcined ZMQ-1 was solved in the orthorhombic space group *Cmmm* (No. 65). The detailed crystallographic data are presented in Table 5.1.

Table 5.1 The crystallographic data of as-made and calcined ZMQ-1.

File name	Calcined ZMQ-1	As-made ZMQ-1
Crystal system	Orthorhombic	Monoclinic
Space Group	$Cmmm$	$P2/m$
a (Å)	18.80(10)	18.94(3)
b (Å)	53.9(2)	20.21(4)
c (Å)	20.55(5)	27.51(7)
α (°)	90	90
β (°)	90	103.56(19)
γ (°)	90	90
Volume	20816(147)	10236(37)
Z	16	4
Wavelength (Å)	0.02508	0.01968
Radiation type	Electron	Electron
Temperature (K)	293(2)	80(2)
Completeness (%)	85.3	77.0
No. of reflections (all unique)	13308	6828
No. of reflections (Fo>4σ(Fo))	61331	77381
Refined parameters	443	446
R_{int}	0.1998	0.3507
R_1 (Fo>2σ(Fo))	0.1997	0.2463
R_1 (all reflections)	0.2708	0.3369
GOF	1.288	1.053

As shown in Figure 5.4a, the structure of calcined ZMQ-1 exhibited an extra-large pore delimited by 28 T-atoms. These extra-large 28-rings are interconnected by 10-rings, forming a 3D 28 × 10 × 10-ring channel system. There are three symmetry-independent 10-ring windows in the framework; each contains two rings and connects two adjacent 28-ring channels. Two windows are perpendicular to *a*-axis: one built by double 10-rings (#1, in cyan) and one by 10-rings and 12-rings (#2, in green). The third one is built from two 10-rings (#3, in blue).

In contrast to most extra-large pore zeolites, which typically exhibit an "interrupted framework", ZMQ-1 is characterized by a fully tetrahedrally connected framework. As shown in Fig. 5.4b, the free pore diameters are 22.32 Å×11.84 Å for the 28-ring channel with 5.74 Å×5.36 Å (#1), 5.44 Å×5.61 Å (#2), 4.60 Å×5.81 Å (#3) for the 10-ring windows. Thus, ZMQ-1 exhibits the largest pore size ever reported among all existing stable zeolites.

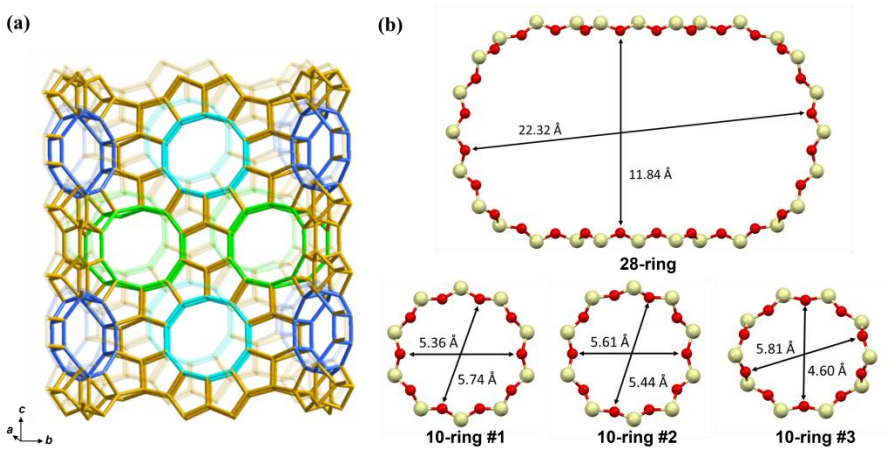

Figure. 5.4 Free diameter of the 28-ring and 10-rings in calcined ZMQ-1, in which the diameter of oxygen (2.70Å) has been subtracted. The figure is reproduced from Lu *et al*. with permission from Springer Nature.

As shown in Figure 5.5, both as-made and calcined ZMQ-1 possesses extra-large 28-ring channels, which were confirmed by STEM images. Notably, in Figure 5.5c, certain atoms in the disordered region appear brighter than those in the surrounding areas. This increased brightness is attributed to the limited resolution of the iDPC image. As a result, these closely spaced atomic columns cannot be individually resolved and instead appear as single, more intense spots. The bright contrast observed in the extra-large pore indicates the presence of disordered molecules. Considering the flexible

cyclohexyl terminal groups within the OSDA molecule, it is likely that these contrasts correspond to disordered OSDAs.

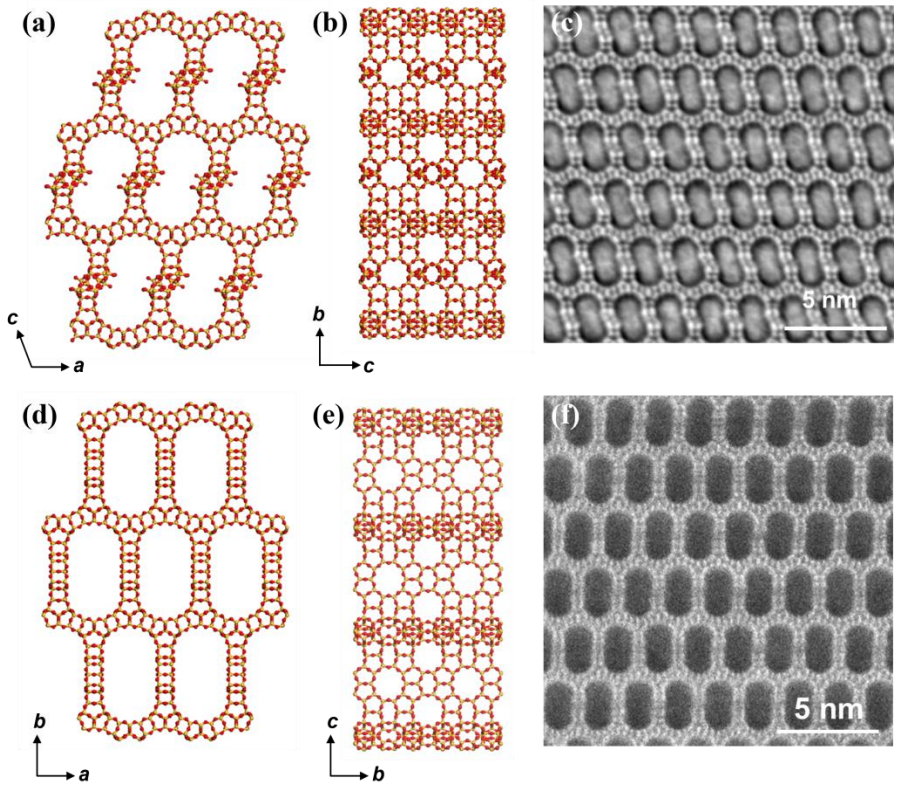

Figure. 5.5 (a,b) The structure of as-made ZMQ-1 with 28-ring channel viewed along the *b*-axis (a) and *a*-axis (b), respectively. (c) iDPC-STEM image of as-made ZMQ-1 taken along the 28-ring channels showing the bilobal-shaped pores. (d, e) The structure of calcined ZMQ-1 with 28-ring channel viewed along the *c*-axis (d) and *a*-axis (e), respectively. (f) ADF-STEM image of calcined ZMQ-1 acquired along the *c*-axis showing the extra-large 28-ring channel. The figure is reproduced from Lu *et al*. with permission from Springer Nature.

Unlike the capsule-shaped mesoporous channel observed in the calcined sample, the as-made ZMQ-1 exhibits a tilted bilobal-shaped channel, with some terminal hydroxyl groups (–OH) pointing towards the channel interior. This structural difference indicates a structural transformation of framework during the calcination process. The specific regions involved in this transformation are illustrated in Figure 5.6, where atoms undergoing bond rearrangement are color-coded. Grey atoms represent sites of bond breakage

during calcination. While atoms highlighted in green, blue, and magenta, each belonging to different chemical building units, indicate regions where bonds were rearranged but remained connected. Together, these colored regions illustrate the framework reorganization that results in a fully connected structure after calcination.

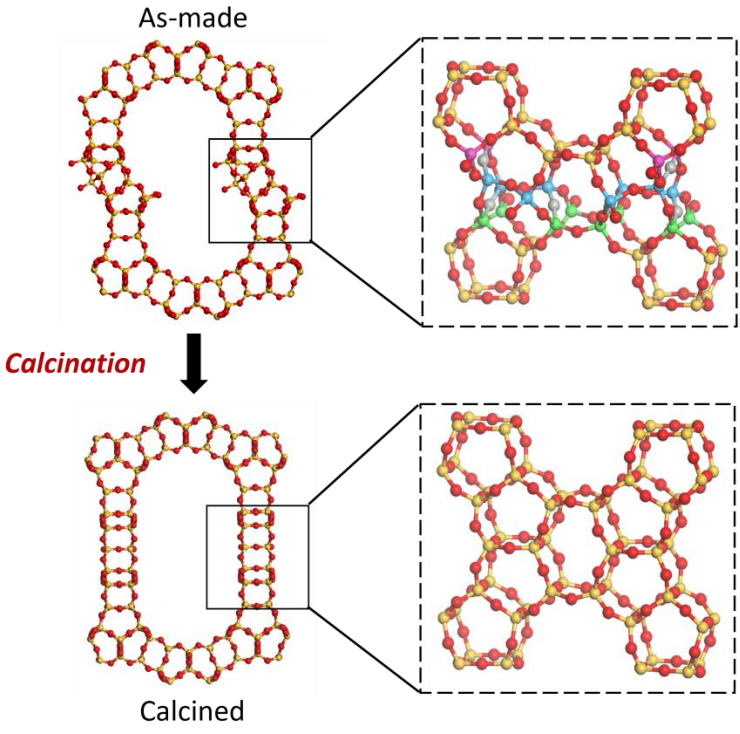

Figure. 5.6 Structural transformation during calcination.

5.1.2 Atomic position determination of OSDAs (Tri-Cy-dC8)

Due to the organic nature of Tri-Cy-dC8 and its weak interaction with the zeolite framework, it is vulnerable to the electron-beam damage. To mitigate the beam-induced degradation of the OSDAs, the low-dose 3DED data (0.0025 $e^{-}/Å^2/s$) was collected under cryogenic conditions (80 K). It is worth noting that the use of a low electron fluence reduced the data resolution from 0.8 Å (obtained at room temperature) to 1.08 Å (under cryogenic conditions). Therefore, the high-resolution framework model of as-made ZMQ-1 solved from the room-temperature data was used as the starting point for refinement against the low-dose cryo-cRED data. The atomic positions of OSDAs were then determined based on the resulting Fourier map. An initial rigid-body

refinement was performed with the framework atoms fixed. Once the OSDA atoms were located from difference electrostatic potential maps, the entire structure was subjected to a full refinement.

Interestingly, the octamethylene chain in each OSDA is interlocked within a 10-ring window, with its tricyclohexylphosphonium heads extending into two different 28-ring channels (Figure 5.7a). These tricyclohexyl groups appeared as broad density regions in the Fourier map, presumably due to their flexibility. This observation is consistent with the iDPC image of the as-made ZMQ-1 (Figure 5.5c). As these groups could not be located based on the Fourier map, they were modelled using Material Studio and incorporated into the structure model after refinement process.

The presence of the positively charged OSDA molecules helps stabilize the terminal –OH groups in the framework. During calcination, the OSDAs decomposed, and the resulting fragments were then removed from the framework through washing. This process eliminates the terminal –OH groups, allowing the interrupted framework to undergo bond rearrangement and formed a fully connected Si–O network. This transformation is supported by the ADF image of the calcined ZMQ-1 (Figure 5.5f), where the absence of significant contrast within the pores indicates the removal of OSDAs.

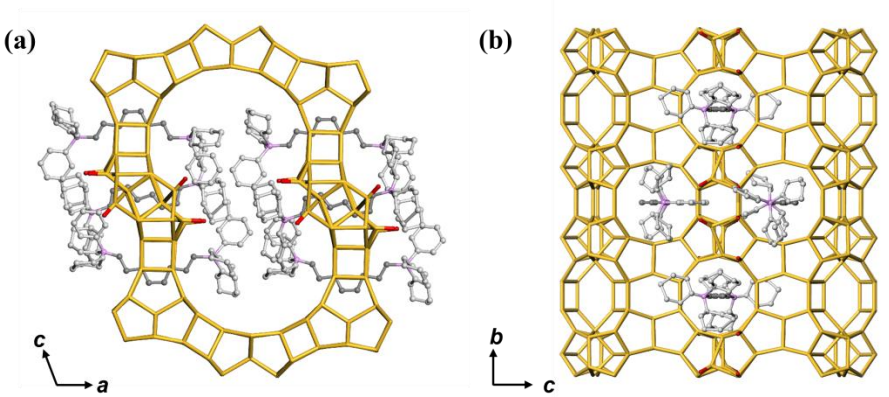

Figure. 5.7 (a) The as-made ZMQ-1 structure viewed along the b-axis, showing OSDA molecules with their tricyclohexylphosphonium heads extending into two different 28-ring channels. (b) A 28-ring channel viewed along the a-axis, highlighting how each OSDA is interlocked within the 10-ring windows that connect adjacent 28-ring channels. The terminal hydroxyl groups condense to form a fully four-connected framework. Color code: purple, phosphorous; dark gray, carbon determined by 3DED data; light gray, carbon generated by chemical information. Only the T···T connections of the framework are shown, and H atoms are omitted for clarity. The figure is reproduced from Lu *et al*. with permission from Springer Nature.

5.2 Structural studies a series of isostructural aluminum monocarboxylates CAU-71-X

Due to the abundance of aluminum (Al) in the crust of Earth, aluminum-based materials are widely synthesized and utilized in various applications, including abrasives[104], catalyst supports[105], and dyeing mordants[106]. Synthetic aluminum compounds encompass a broad range of materials, such as aluminum oxides/hydroxides[107,108], zeolites, and metal-organic frameworks (MOFs)[109]. Among these, aluminum carboxylates have attracted significant attention in recent decades, particularly in the development of MOFs incorporating polycarboxylate ligands. With tunable porosity and readily available starting materials, Al-based MOFs have emerged as promising candidates for gas storage/separation[110] and heat exchange[111].

Despite their long industrial history, systematic studies on porous aluminum monocarboxylates derived from simple monocarboxylic acids remain limited.[112–115] Many short-chain monocarboxylic acids, such as formic acid, acetic acid, and glycolic acid, are naturally occurring and can be derived from renewable resources. Their abundance, low cost, and often non-toxic nature make them promising ligands for synthesizing Al-based materials. In this study, a series of Al-based MOFs were synthesized by using different monocarboxylic acids (Figure 5.8). For convenience, the resulting compounds were denoted as CAU-71-X, where X = Ac, Prop and TGA.

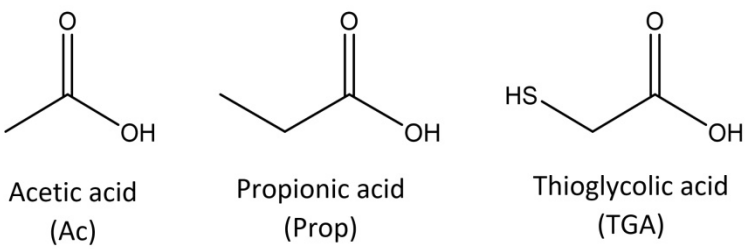

Figure. 5.8 The monocarboxylic acids used for the synthesis of CAU-71-X with X = Ac, Prop and TGA.

As shown in Figure 5.9, the PXRD patterns of CAU-71-Xs exhibit high similarity, indicating the formation of isostructural frameworks. These materials were obtained as nano- to micro-crystals, thereby the structure determination was carried out by 3DED. However, the high flexibility of the ligands complicated the structural analysis, making it difficult to accurately determine the terminal atoms of the ligands. To achieve completed structure determination, the low-dose cryo-cRED method was employed to stabilize the

structure CAU-71-Xs during data collection. This approach not only enabled accurate structure determination but also allowed for the refinement of positional disorder in the CAU-71 frameworks.

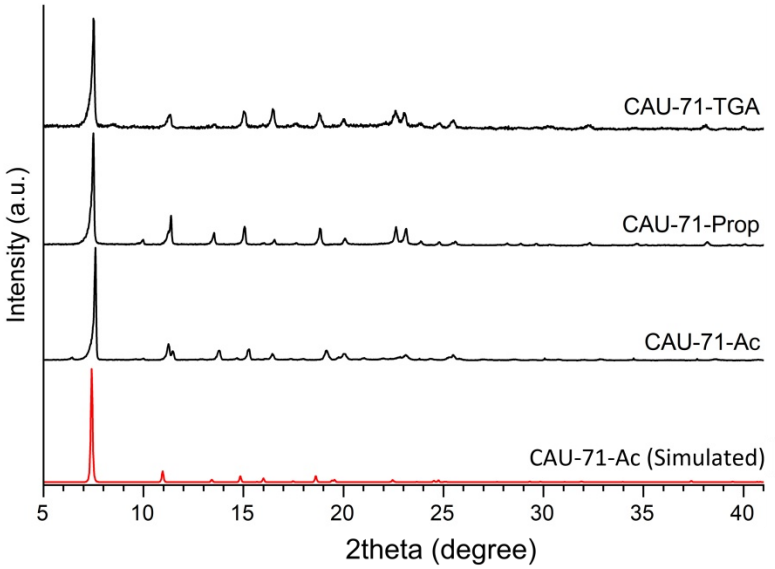

Figure 5.9. Measured PXRD patterns of CAU-71-X with X = Ac, Prop and TGA. For comparison, the simulated PXRD pattern of CAU-71-Ac, based on the structure model solved by 3DED, is also shown.

5.2.1 Structures of CAU-71-Xs

The CAU-71-X crystallized in the trigonal space group *R*-3 (No. 148) with similar unit cell parameters, as summarized in Table 5.3. Due to the structural similarity among the isostructural CAU-71-X compounds, the structure of CAU-71-Ac is selected as a representative example to illustrate the detailed structural features.

A distinctive feature of the structure is the presence of an 18-ring with an inner diameter of 8.97 Å (measured by the C1…C1 distance) as shown in Figure 5.10b. The 18-ring is alternately assembled by two distinct inorganic building units (IBUs): a single $Al(OH)_2(OR)_4$ octahedron (Figure 5.10c) and a μ_3-oxo-centred Al-trimer consisting of three edge-sharing $Al(O/OH)(OH)_3(OR)_2$ octahedra (Figure 5.10d). The Al-trimers are located at the honeycomb lattices, bridged by the $Al(OH)_2(OR)_4$ octahedral units to form a 18-ring honeycomb layer (Figure5.10a-b). As shown in Figure 5.10e, the Al-

trimer cluster is interconnected with $Al(OH)_2(OR)_4$ octahedron by one corner-sharing oxygen atom and two bidentate acetate ligands, of which each oxygen atom coordinates to an Al^{3+} ion from both IBUs. In total, this 18-ring consists of 18 [AlO_6] octahedra and 24 bidentate acetate ligands (Figure 5.10a). Among the 24 acetate ligands, each six are oriented to the central, periphery, above and below of the ring. The 18 Al^{3+} ions exhibit a circular zigzag configuration along *c*-axis (Figure 5.10b) and are connected in a hexagonal arrangement within the *ab*-plane, giving rise to a two-dimensional porous layer structure. The resulting zigzag layers interact via interlayer hydrogen bonding, leading to the formation of a three-dimensional crystalline structure with ABC stacking (Figure 5.11). As shown in Figure 5.12, the interlayer hydrogen bonds are formed between the hydroxyl groups (-OH) and the oxygen atoms of the Al-trimer from adjacent layers.

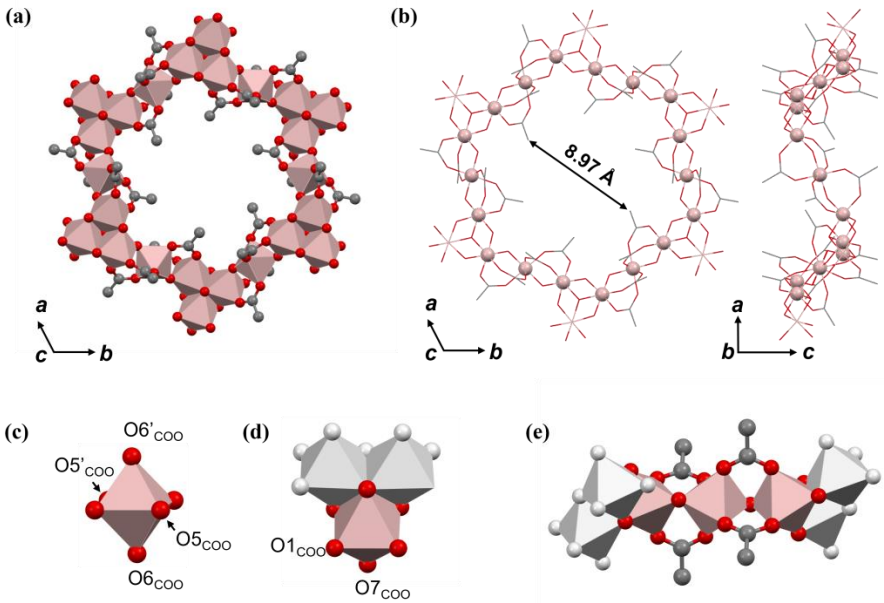

Figure. 5.10 (a) The 18-ring in CAU-71-Ac viewed along the *c*-axis and (b) the zigzag configuration 18 Al^{3+} ion. (c) The polyhedral model of $Al(OH)_2(OR)_4$ octahedral building unit. (d) The polyhedral model of Al-trimer. (e)The interconnection of IBUs within 18-ring. Color code: pink, aluminum; dark gray, carbon; red, oxygen; light grey, the symmetry-generated Al octahedra. The carboxylate oxygen atoms are labeled as O_{COO}. The size of the 18-ring in (b) is represented by the C…C distance.

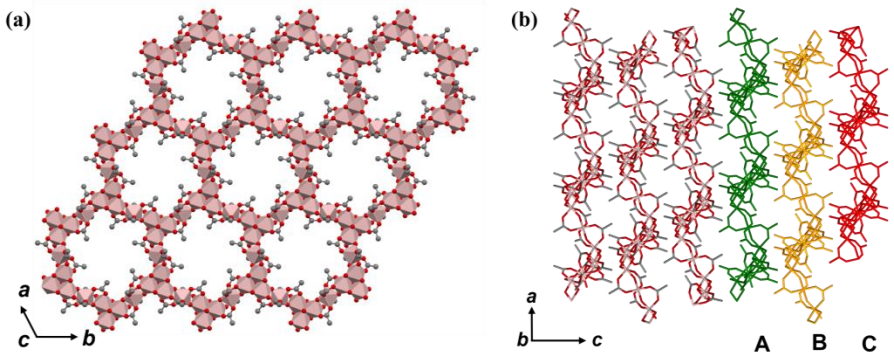

Figure. 5.11 (a) 2D porous layer of CAU-71-Ac view along *c*-axis, and (b) the corresponding ABC stacking view along *b*-axis.

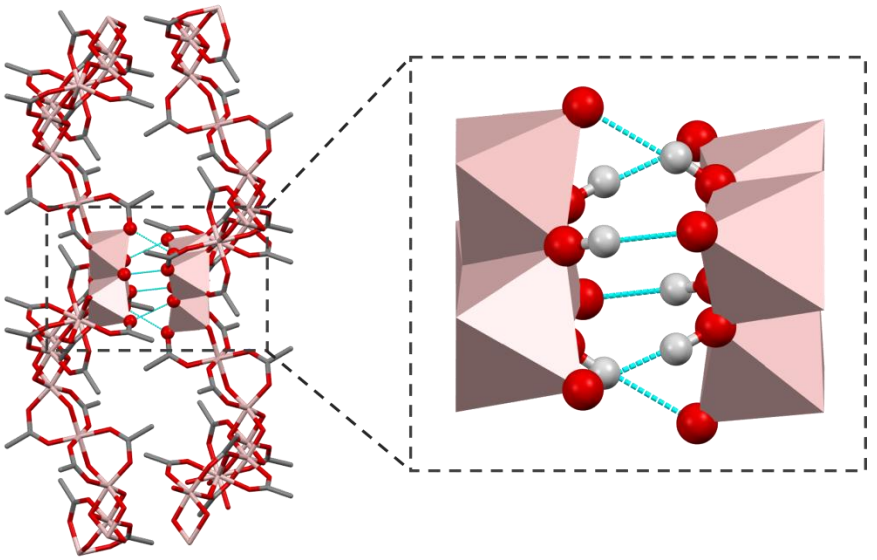

Figure. 5.12 The interlayer interaction via hydrogen bonding view along *b*-axis.

The 18-ring of CAU-71-Prop and CAU-71-TGA are shown in Figure 5.13. Similarly, the honeycomb layers in CAU-71-Prop and CAU-71-TGA are also interacted via the interlayer hydrogen bonding, packed in ABC stacking, as summarized in Table 5.2. The low-dose cryo-cRED method enabled the identification of all non-H atoms in the structures, including the highly flexible organic ligands. This allows to distinguish the three isostructures, which was

not possible when cRED data were collected by only reducing electron fluence or applying cryo-protection alone.

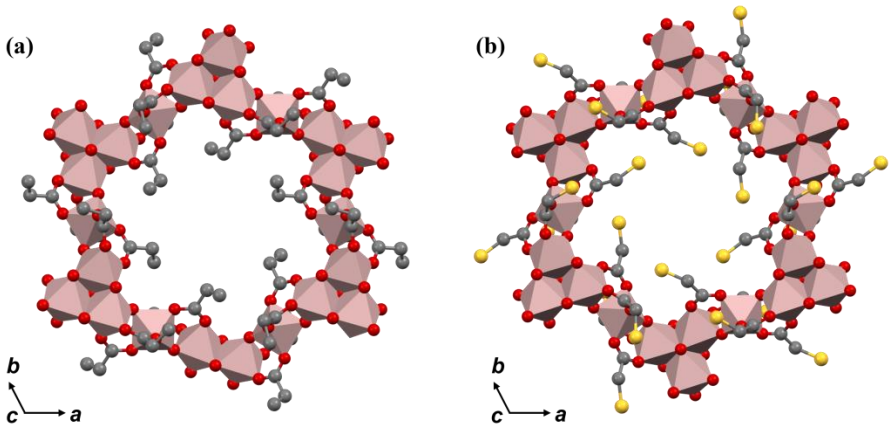

Figure. 5.13 The 18-ring of (a) CAU-71-Prop and (b) CAU-71-TGA view along the *c*-axis.

Material	D–H···A	Distance (Å)
CAU-71-Ac	O3–H···O7	2.87(1)
CAU-71-Prop	O4–H4···O12	2.88(1)
CAU-71-TGA	O9–H9···O7	2.96(2)

Table. 5.2 The summary of the interlayer hydrogen bonding for CAU-71-Ac, CAU-71-Prop, and CAU-71-TGA.

Table 5.3 The crystallographic data and refinement statistics of CAU-71-Ac, CAU-71-Prop, and CAU-71-TGA.

File name	CAU-71-Ac	CAU-71-Prop	CAU-71-TGA
Chemical Formula	$C_{24}H_{51}Al_9O_{39}$	$C_{36}H_{37}Al_9O_{40.93}$	$C_{24}H_{37}Al_9O_{40.45}S_{12}$
Formula weight	1206.47	1367.37	1600.07
Crystal system	Trigonal	Trigonal	Trigonal
Space Group	R-3	R-3	R-3
a (Å)	15.11(3)	15.290(2)	15.335(5)
b (Å)	15.11(3)	15.290(2)	15.335(5)
c (Å)	23.36(3)	23.08(3)	23.441(15)
α (°)	90	90	90
β (°)	90	90	90
γ (°)	120	120	120
Volume	4619(20)	4672(5)	4774(4)
Z	6	6	6
Wavelength (Å)	0.02508	0.01968	0.01968
Radiation type	Electron	Electron	Electron
Temperature (K)	95(2)	80(2)	80(2)
Completeness (%)	98.6	88.6	89.6
No. of reflections (all unique)	1585	1623	1063
No. of reflections (Fo>4σ(Fo))	7570	11760	7048
Refined parameters	127	158	166
R_{int}	0.2083	0.2552	0.2903
R_1 (Fo>2σ(Fo))	0.1803	0.1703	0.1663
R_1 (all reflections)	0.2375	0.2399	0.2670
GOF	1.144	1.040	1.071

6. Summary

This thesis advances the application of 3DED for the structure determination of beam-sensitive materials, with a focus on pharmaceuticals, zeolites, and metal-organic frameworks. Through four case studies, we demonstrate tailored strategies to minimize the electron-beam damage during 3DED experiments. These strategies include: (1) low electron fluence, (2) cryo-cooling, and (3) the low-dose cryo-cRED method, which combines both strategies. Furthermore, a cryo-sample preparation workflow was developed to address materials that are sensitive to both the electron beam and moisture.

We discovered two piroxicam (PXM) polymorphs (form VIII and form IX) through polyethylene glycol (PEG)-assisted melt crystallization and their structures were determined from 3DED data collected under low electron fluence at room temperature. To achieve this, experimental parameters related to electron flux (including condenser aperture and condenser lens) and recording time (including rotation speed and rotation range) were adjusted to reduce the cumulative electron fluence per dataset. The structure information, provided insights into the distinct difference in melting points between the two polymorphs (form IV and form VIII) that have similar packing but different intermolecular hydrogen-bonding.

We reported the first structure of anhydrous sodium valproate determined by cryo-cRED. To address the sensitivity of anhydrous sodium valproate to both electron and moisture, a glovebox assisted cryo-sample preparation workflow was developed, enabling the plunge-freezing of the sample under a humidity-free atmosphere. While the glovebox prevented the dissolution of the crystals by moisture during sample preparation, the cryo-protection safeguarded the sample from the electron-beam damage during data collection.

We determined the atomic structure of ZMQ-1, the first stable aluminosilicate zeolite with an intrinsic meso-microporous channel system—a groundbreaking discovery in the field of zeolites. The framework structures of both calcined and as-made samples were determined using 3DED data obtained at room temperature. The structures of ZMQ-1 not only revealed their 28-ring mesopore with a free diameter of 22.76 Å × 11.83 Å, but also provided insights into the structure rearrangement occurring during the calcination process. To gain deeper insights into the formation of the mesoporous channel, it is essential to determine the atomic position of OSDAs within as-made ZMQ-1. The location of the OSDAs could be achieved when the low-dose cryo-cRED method was employed to stabilize OSDA molecules and minimize electron-beam damage. This combined approach enabled the precise localization of OSDA within the pores of the zeolite framework.

Finally, we studied a series of aluminium carboxylates synthesized using monocarboxylic acids. Three layered isostructural aluminium monocarboxylates CAU-71 (X = Ac, Prop, TGA) were discovered. The combined low-dose cryo-cRED approach not only enabled complete determination the isostructural CAU-71-Xs, but also allowed proper refinement of positional disorder of the ligand atoms. The structures of CAU-71-X consist of unique honeycomb-like layers with 18-rings, which are further packed into a 3D structure through interlayer hydrogen bonding. The low-dose cryo-cRED method enabled the differentiation of highly flexible organic ligands among the three isostructural variants, which was not achievable by only reducing electron fluence or applying cryo-protection alone.

In conclusion, the strategies and workflow developed in this thesis have expanded the application of 3DED to beam-sensitive crystalline materials. These methods enhance the reliability of 3DED and provide new pathways for structural studies, offering valuable insights into materials that are challenging for traditional techniques.

7. Future perspectives

The developments presented in this thesis demonstrate the power of 3DED for the structural determination of beam-sensitive crystalline materials. However, challenges still exist, and further advancements are needed to enhance the accuracy and applicability of 3DED.

First of all, although 3DED data collection has become more routine, with everyone having their preferred default settings, it is still crucial to emphasize the importance of minimizing pre-irradiation. Besides blanking the electron beam used in this thesis, as we discussed earlier, another approach is using a low electron flux during alignment and crystal selection. One notable example is the Electrostatic Dose Modulator (EDM) developed by JEOL. By employing a fast electrostatic deflector, the EDM enables beam blanking in under 2 μs (500 kHz), significantly outperforming traditional magnetic shutters. This technology allows independent control of beam intensity without altering imaging conditions, making it particularly suitable for studying beam-sensitive materials. Users can precisely regulate electron dose by applying pulses with adjustable durations as short as 100 ns and frequencies up to 500 kHz. Furthermore, the EDM integrates seamlessly into existing TEM systems and features intuitive software control, allowing smooth incorporation into the 3DED workflow. ThermoFisher Scientific implemented NanoPulser on their new STEM, which is an electrostatic beam blanker that can optimize the electron dose and run time-resolved experiments. These solutions not only enhance experimental flexibility but also improve overall data quality.

In addition to hardware advancements, alternative data collection techniques can also help mitigate electron-beam damage. One such approach is serial electron diffraction (SerialED). The continuous SerialED recently developed in our group collects data by capturing a single diffraction frame from each crystal while continuously moving the grid, which is densely populated with crystalline material, across the electron beam. Sampling a large number of crystals with varying orientations enables effective reconstruction of the 3D reciprocal lattice. This process ensures that each crystal is exposed to the beam for only a very short time, minimizing cumulative electron-beam damage. Additionally, this method allows the use of a high electron flux, which improves the signal-to-noise ratio, further enhancing data quality for structural analysis.

Beyond these perspectives on the future of 3DED method, the advancements presented in this thesis pave the way for its application to a broader range of materials. Specifically, the sample preparation workflows developed in this thesis provides opportunity for applying 3DED analysis to materials with strict requirement to surrounding environment. For instance,

most polymorphs of sodium valproate still remain unsolved, primarily due to their sensitivity to humidity. This workflow makes structure determination possible for these polymorphs by 3DED. Similarly, the method§ could be applied to battery materials, which require protection from ambient oxygen and moisture during structural analysis.

Furthermore, this sample preparation method can also be extended to study the structural evolution during chemical reactions. By carefully controlling the surrounding atmosphere of sample, we can capture real-time changes in the structure of a material as it undergoes transformation. This approach is particularly useful for trapping reaction intermediates, enabling high-resolution analysis of transient species that might otherwise be difficult to observe.

Finally, it was observed that some MOFs exhibited high-resolution diffraction on synchrotron radiation but failed to diffract during 3D ED analysis. This may attribute to the vacuum environment in the electron microscope, which could potentially damage the crystalline porous structure of MOFs. One potential solution is to plunge-freeze the sample before loading it into the TEM. The low temperature (around 95 K) helps stabilize the guest molecules within the pores, preventing the collapse of the porous structure. However, in our previous work, this approach did not yield the desired results. To overcome this challenge, exploring the use of environmental transmission electron microscopy (ETEM) for 3DED analysis could be a promising alternative. ETEM allows for the observation specimens under a gas-controlled environment, which may help to preserve the structural integrity of samples during the 3DED experiment.

Populärvetenskaplig sammanfattning

Tredimensionell elektrondiffraktion (3DED) har blivit ett viktigt verktyg för strukturbestämning av nano- och mikroskopiska kristaller. Metoden erbjuder unika möjligheter att undersöka material på mikroskopisk nivå, men den stöter på ett stort hinder: strålningsskador. När en elektronstråle interagerar med ett material kan det orsaka strukturella skador som försämrar datakvaliteten och försvårar möjligheten att fastställa den korrekta strukturen – särskilt när det gäller strålkänsliga material såsom zeoliter, metall-organiska ramverk (MOF:er) och läkemedelskristaller. För att lösa detta problem har jag använt flera strategier för att skydda materialen under datainsamlingen. Dessa inkluderar kylning, användning av låg elektrondos och särskilda provberedningsmetoder. Genom dessa tillvägagångssätt har materialens strukturella integritet kunnat bevaras, vilket i sin tur förbättrar tillförlitligheten hos 3DED-data.

Denna avhandling undersöker fyra strålkänsliga material med hjälp av 3DED och utvecklar anpassade strategier för att minimera strålningsskador. Flera nya protokoll för provberedning och datainsamling har tagits fram för att vidga tillämpningen av 3DED till en bredare uppsättning material. Ett exempel är piroxicam, ett icke-steroidalt antiinflammatoriskt läkemedel. Vi upptäckte två nya polymorfer och bestämde deras strukturer genom att optimera datainsamlingsparametrar för att minska skador från elektronstrålen. Natriumvalproat är ett av de mest effektiva antiepileptiska läkemedlen, men strukturen hos dess vattenfria form har tidigare inte kunnat klarläggas på grund av dess extrema känslighet för både strålning och fukt. Vi lyckades bestämma denna struktur med hjälp av kryo-3DED. En särskilt utformad glovebox med inert atmosfär användes för att förbereda kryoprov för att bevara strukturen.

Vidare upptäckte vi nya porösa material: zeoliten ZMQ-1 och det metallorganiska ramverket CAU-71. ZMQ-1 är den första stabila aluminosilikatzeoliten med ett inbyggt meso-mikroporöst kanalsystem. CAU-71 består av unika porösa bikakeliknande skikt. Vi utvecklade låg-dos kryo-3DED för att stabilisera känsliga strukturdelar och flexibla grupper i organiska ligander. Detta gjorde det möjligt att fastställa högupplösta strukturer även för material som annars skulle vara för känsliga för traditionell 3DED.

Sammanfattningsvis presenterar denna avhandling en rad strategier för att hantera strålningsskador och miljökänslighet hos strålkänsliga prover. Genom att utveckla dessa metoder utökas användningen av 3DED, vilket öppnar nya möjligheter för strukturella studier – särskilt för material som är känsliga för elektronstrålar och miljöfaktorer. Resultaten från denna forskning ger värdefulla insikter inom både materialvetenskap och farmaceutisk utveckling.

Acknowledgements

First and foremost, I would like to express my deepest gratitude to my supervisor, Professor Xiaodong Zou. Your invaluable guidance, continuous support, and encouragement have shaped my PhD journey in countless ways. Your expertise and dedication have not only helped me overcome scientific challenges but also nurtured my growth as an independent researcher. I am truly grateful for your insightful advice and unwavering belief in my potential, which have been instrumental in my academic and personal development.

I am also sincerely grateful to my co-supervisor, Dr. Hongyi Xu. Your insightful discussions and support have provided me with fresh perspectives and inspiration throughout my research. Beyond research, you have also supported me in many aspects of life, your kindness and generosity have made a significant difference in my PhD experience. I also extend my sincere thanks to Dr. Taimin Yang. Although our time working together was short, the knowledge you shared, especially in software and technical aspects, has been immensely valuable.

To all my colleagues in MMK (which is Kemikum now), I am deeply appreciative of your support and guidance, which have made my time at Stockholm University both fulfilling and enjoyable. Special thanks to Dr. Andrew Kentaro Inge, Drs. Tom Willhammar, Yu Xia, Cheuk Wai Tai, Yinlin Chen, and Anumol Ashok for your timely assistance and patient training.

I also want to thank my office mates over the years—Jingjing, Molly, Paul, Ed, Bernadette, Tra Mi, and Linda—for creating such a warm and friendly work environment. My gratitude also extends to my previous and current group members: Dr. Guojun Zhou, Dr. Yi Luo, Dr. Meng Ge, Dr. Hui Wang, Dr. Jung Cho (James), Dr. Zhehao Huang, Dr. Gerhard Hofer, Laura Pacoste, Lei Wang, Shihui Feng, Sofiia Butonova, Evgeniia Ikonnikova, Dr. Lesya Demchenko, Angelina Vypritskaia, Branislav Jeriga, Dr. Walter Wong, Zheting Chu, Lyu Jia, Yan Zheng, Dr. Jianbo Song, Dr. Ioannis Mylonas-Margaritis, and Dr. Huiqiu Wang. Whether through scientific discussions or everyday interactions, I have learned so much from each of you.

I would also like to acknowledge my collaborators. Dr. Changlin Yao from Ludong University, your expertise in melt crystallization and polymorphism has been indispensable to our collaboration. I am sincerely grateful for your support and trust in my contributions.

My thanks also go to Professor Peng Lu and Yiqing Sun from Qingdao New Energy Shandong Laboratory, as well as Professor Valentin Valtchev from Normandie University. Your efforts in synthesizing ZMQ-1, the largest-pore stable zeolite reported to date, were critical to our project. This work

demanded immense dedication, and I am truly appreciative of the challenges we overcame together, leading to our shared success.

I am also grateful to Professor Changquan Calvin Sun from the University of Minnesota for providing the pharmaceutical samples, as well as Dr. Vivek Srinivas and Professor Martin Högbom from Stockholm University for their invaluable help in sample preparation. Your generosity in lending us the glovebox and assisting with sample handling significantly contributed to our work.

I want to express my appreciation to Dr. Bastian Achenbach and Professor Norbert Stock from Christian-Albrechts-Universität zu Kiel. Collaborating with you on my final PhD project was an enriching experience, and your timely support was essential in ensuring its successful completion. I deeply value your dedication and assistance.

Last but certainly not least, I want to thank my family and dear friends. Your constant support and understanding have been my greatest source of strength. I am profoundly grateful for your love and encouragement. You have stood by me during the most challenging times, and your unwavering belief in me has made all the difference.

References

1. Verlag GmbH, W. & KGaA, C. *Physical Properties of Crystals An Introduction*.
2. Bunaciu, A. A., Udriştioiu, E. gabriela & Aboul-Enein, H. Y. X-Ray Diffraction: Instrumentation and Applications. *Critical Reviews in Analytical Chemistry* vol. 45 289–299 Preprint at https://doi.org/10.1080/10408347.2014.949616 (2015).
3. Inokuma, Y. *et al.* X-ray analysis on the nanogram to microgram scale using porous complexes. *Nature* **495**, 461–466 (2013).
4. Gruene, T. *et al.* Rapid Structure Determination of Microcrystalline Molecular Compounds Using Electron Diffraction. *Angewandte Chemie* **130**, 16551–16555 (2018).
5. Le Pevelen, D. D. Small Molecule X-Ray Crystallography, Theory and Workflow. *Encyclopedia of Spectroscopy and Spectrometry* 2559–2576 (2010) doi:10.1016/B978-0-12-374413-5.00359-6.
6. Harris, K. D. M., Tremayne, M. & Kariuki, B. M. Contemporary advances in the use of powder X-ray diffraction for structure determination. *Angewandte Chemie - International Edition* vol. 40 1626–1651 Preprint at https://doi.org/10.1002/1521-3773(20010504)40:9<1626::aid-anie16260>3.0.co;2-7 (2001).
7. Zou, X., Hovmöller, S. & Oleynikov, P. *Electron Crystallography: Electron Microscopy and Electron Diffraction*. vol. 16 (Oxford University Press, 2011).
8. Gemmi, M. & Lanza, A. E. 3D electron diffraction techniques. *Acta Crystallogr B Struct Sci Cryst Eng Mater* **75**, 495–504 (2019).
9. Li, J. & Sun, J. Application of X-ray Diffraction and Electron Crystallography for Solving Complex Structure Problems. *Acc Chem Res* **50**, 2737–2745 (2017).
10. Duyvesteyn, H. M. E. *et al.* Machining protein microcrystals for structure determination by electron diffraction. *Proc Natl Acad Sci U S A* **115**, 9569–9573 (2018).
11. Palatinus, L. *et al.* Hydrogen positions in single nanocrystals revealed by electron diffraction. *Science (1979)* **355**, 166–169 (2017).
12. Smeets, S., Ångström, J. & Olsson, C. O. A. Quantitative Phase Analysis for Carbide Characterization in Steel Using Automated Electron Diffraction. *Steel Res Int* **90**, 1–7 (2019).
13. Lightowler, M. *et al.* Phase Identification and Discovery of an Elusive Polymorph of Drug-Polymer Inclusion Complex Using Automated 3D Electron Diffraction. *Angewandte Chemie - International Edition* **63**, (2024).
14. Egerton, R. F. Radiation damage to organic and inorganic specimens in the TEM. *Micron* vol. 119 72–87 Preprint at https://doi.org/10.1016/j.micron.2019.01.005 (2019).
15. Egerton, R. F., Li, P. & Malac, M. Radiation damage in the TEM and SEM. in *Micron* vol. 35 399–409 (2004).
16. Egerton, R. F. Mechanisms of radiation damage in beam-sensitive specimens, for TEM accelerating voltages between 10 and 300 kV. *Microsc Res Tech* **75**, 1550–1556 (2012).
17. Chen, Q. *et al.* Imaging Beam-Sensitive Materials by Electron Microscopy. *Advanced Materials* vol. 32 Preprint at https://doi.org/10.1002/adma.201907619 (2020).
18. Zhan, Z. *et al.* Atomic-level imaging of beam-sensitive COFs and MOFs by low-dose electron microscopy. *Nanoscale Horizons* vol. 9 900–933 Preprint at https://doi.org/10.1039/d3nh00494e (2024).

19. Puster, M., Rodríguez-Manzo, J. A., Balan, A. & Drndić, M. Toward sensitive graphene nanoribbon-nanopore devices by preventing electron beam-induced damage. *ACS Nano* **7**, 11283–11289 (2013).
20. Williams, D. B. & Carter, C. B. *Transmission Electron Microscopy*. (Springer US, Boston, MA, 1996). doi:10.1007/978-1-4757-2519-3.
21. Egerton, R. F. Control of radiation damage in the TEM. *Ultramicroscopy* **127**, 100–108 (2013).
22. Xu, J. *et al.* Unveiling the Structure of Anhydrous Sodium Valproate with 3D Electron Diffraction and a Facile Sample Preparation Workflow. Preprint at https://doi.org/10.26434/chemrxiv-2025-8qxqp (2025).
23. Xu, J. *et al.* Polyethylene Glycol-Assisted Melt Crystallization of Two New Piroxicam Polymorphs Revealed by 3D Electron Diffraction. *Cryst Growth Des* **24**, 7298–7305 (2024).
24. Lu, P. *et al.* A stable zeolite with atomically ordered and interconnected mesopore channel. *Nature* **636**, 368–373 (2024).
25. Anosova, O., Kurlin, V. & Senechal, M. The importance of definitions in crystallography. *IUCrJ* **11**, 453–463 (2024).
26. Shull, C. G. & Wilkinson, M. K. Neutron Diffraction Studies of Various Transition Elements. *Rev Mod Phys* **25**, 100–107 (1953).
27. Egami, T. & Billinge, S. J. *Underneath the Bragg Peaks: Structural Analysis of Complex Materials*. vol. 16 (Elsevier, 2003).
28. Maiwald, L. *et al.* Ewald sphere construction for structural colors. *Opt Express* **26**, 11352 (2018).
29. Spence, J. C. H. & Zuo, J. M. *Electron Microdiffraction*. *Electron Microdiffraction* (Springer US, 1992). doi:10.1007/978-1-4899-2353-0.
30. Patterson, A. L. A Fourier Series Method for the Determination of the Components of Interatomic Distances in Crystals. *Physical Review* **46**, 372–376 (1934).
31. Wilson, A. J. C. Solution of the Phase Problem. I. The Centrosymmetric Crystal by H. Hauptman and J. Karle. *Acta Crystallogr* **7**, 384–384 (1954).
32. Sheldrick, G. M. SHELXT - Integrated space-group and crystal-structure determination. *Acta Crystallogr A* **71**, 3–8 (2015).
33. Sheldrick, G. M. A short history of *SHELX*. *Acta Crystallogr A* **64**, 112–122 (2008).
34. McCoy, A. J. *et al.* Phaser crystallographic software. *J Appl Crystallogr* **40**, 658–674 (2007).
35. Burla, M. C. *et al.* Crystal structure determination and refinement via SIR2014. *J Appl Crystallogr* **48**, 306–309 (2015).
36. Altomare, A. *et al.* SIR92 – a program for automatic solution of crystal structures by direct methods. *J Appl Crystallogr* **27**, 435–435 (1994).
37. Palatinus, L. & Chapuis, G. SUPERFLIP - A computer program for the solution of crystal structures by charge flipping in arbitrary dimensions. *J Appl Crystallogr* **40**, 786–790 (2007).
38. Trueblood, K. N. *et al. Atomic Displacement Parameter Nomenclature Report of a Subcommittee on Atomic Displacement Parameter Nomenclaturet*. *770 Acta Cryst* vol. 52 (1996).
39. Sheldrick, G. M. Crystal structure refinement with SHELXL. *Acta Crystallogr C Struct Chem* **71**, 3–8 (2015).
40. Hübschle, C. B., Sheldrick, G. M. & Dittrich, B. ShelXle: A Qt graphical user interface for SHELXL. *J Appl Crystallogr* **44**, 1281–1284 (2011).

41. Müller, P., Herbst-Irmer, R., Spek, A. L., Schneider, T. R. & Sawaya, M. R. *Crystal Structure Refinement*. (Oxford University PressOxford, 2006). doi:10.1093/acprof:oso/9780198570769.001.0001.
42. Kolb, U., Gorelik, T., Kübel, C., Otten, M. T. & Hubert, D. Towards automated diffraction tomography: Part I-Data acquisition. *Ultramicroscopy* **107**, 507–513 (2007).
43. Zhang, D., Oleynikov, P., Hovmoller, S. & Zou, X. Collecting 3D electron diffraction data by the rotation method. *Zeitschrift fur Kristallographie* **225**, 94–102 (2010).
44. Wan, W., Sun, J., Su, J., Hovmöller, S. & Zou, X. Three-dimensional rotation electron diffraction: Software RED for automated data collection and data processing. *J Appl Crystallogr* **46**, 1863–1873 (2013).
45. Nannenga, B. L. & Gonen, T. The cryo-EM method microcrystal electron diffraction (MicroED). *Nature Methods* vol. 16 369–379 Preprint at https://doi.org/10.1038/s41592-019-0395-x (2019).
46. Gemmi, M., La Placa, M. G. I., Galanis, A. S., Rauch, E. F. & Nicolopoulos, S. Fast electron diffraction tomography. *J Appl Crystallogr* **48**, 718–727 (2015).
47. Wang, Y. *et al.* Elucidation of the elusive structure and formula of the active pharmaceutical ingredient bismuth subgallate by continuous rotation electron diffraction. *Chemical Communications* **53**, 7018–7021 (2017).
48. Egerton, R. F. Radiation damage to organic and inorganic specimens in the TEM. *Micron* vol. 119 72–87 Preprint at https://doi.org/10.1016/j.micron.2019.01.005 (2019).
49. Zhang, D. *et al. Atomic-Resolution Transmission Electron Microscopy of Electron Beam-Sensitive Crystalline Materials*. https://www.science.org.
50. INOKUTI, M. Inelastic Collisions of Fast Charged Particles with Atoms and Molecules—The Bethe Theory Revisited. *Rev Mod Phys* **43**, 297–347 (1971).
51. Li, Y., Kang, D. D., Dai, J. Y. & Wang, L. W. The cage effect of electron beam irradiation damage in cryo-electron microscopy. *NPJ Comput Mater* **10**, (2024).
52. Egerton, R. F., Li, P. & Malac, M. Radiation damage in the TEM and SEM. in *Micron* vol. 35 399–409 (2004).
53. Garman, E. F. Radiation damage in macromolecular crystallography: What is it and why should we care? *Acta Crystallogr D Biol Crystallogr* **66**, 339–351 (2010).
54. Ugurlu, O. *et al.* Radiolysis to knock-on damage transition in zeolites under electron beam irradiation. *Phys Rev B Condens Matter Mater Phys* **83**, (2011).
55. Unge, J., Lin, J., Weaver, S. J., Sae Her, A. & Gonen, T. Compositional Analysis of Complex Mixtures using Automatic MicroED Data Collection. *Advanced Science* **11**, (2024).
56. Yang, Q. *et al.* Unified transmission electron microscopy with the glovebox integrated system for investigating air-sensitive two-dimensional quantum materials. *Innovation* vol. 6 Preprint at https://doi.org/10.1016/j.xinn.2024.100751 (2025).
57. Motaln, K. *et al.* Reactive Noble-Gas Compounds Explored by 3D Electron Diffraction: XeF2-MnF4 Adducts and a Facile Sample Handling Procedure. *ACS Cent Sci* (2024) doi:10.1021/acscentsci.4c00815.
58. Cichocka, M. O., Ångström, J., Wang, B., Zou, X. & Smeets, S. High-throughput continuous rotation electron diffraction data acquisition via software automation. *J Appl Crystallogr* **51**, 1652–1661 (2018).
59. Smeets, S., Zou, X. & Wan, W. Serial electron crystallography for structure determination and phase analysis of nanocrystalline materials. *J Appl Crystallogr* **51**, 1262–1273 (2018).
60. Kabsch, W. XDS. *Acta Crystallogr D Biol Crystallogr* **66**, 125–132 (2010).

61. Girolami, G. S. *A Guide to Using the SHELXTL Crystallographic Software Package XSHELL Version*. (2004).
62. Spek, A. L. CheckCIF validation ALERTS: What they mean and how to respond. *Acta Crystallogr E Crystallogr Commun* **76**, 1–11 (2020).
63. Watkin, D. Structure refinement: some background theory and practical strategies. *J Appl Crystallogr* **41**, 491–522 (2008).
64. Bernstein, J. *Polymorphism in Molecular Crystals*. (Oxford University Press, 2020). doi:10.1093/oso/9780199655441.001.0001.
65. Cruz-Cabeza, A. J. & Bernstein, J. Conformational polymorphism. *Chem Rev* **114**, 2170–2191 (2014).
66. Aitipamula, S. *et al.* Polymorphs, Salts, and Cocrystals: What's in a Name? **12**, 2021 (2012).
67. Shi, Q. *et al.* Recent advances in drug polymorphs: Aspects of pharmaceutical properties and selective crystallization. *Int J Pharm* **611**, 121320 (2022).
68. Chen, S., Guzei, I. A. & Yu, L. New polymorphs of ROY and new record for coexisting polymorphs of solved structures. *J Am Chem Soc* **127**, 9881–9885 (2005).
69. Shtukenberg, A. G. *et al.* Melt Crystallization for Paracetamol Polymorphism. *Cryst Growth Des* **19**, 4070–4080 (2019).
70. Ou, X., Li, X., Rong, H., Yu, L. & Lu, M. A general method for cultivating single crystals from melt microdroplets. *Chemical Communications* **56**, 9950–9953 (2020).
71. Li, X. *et al.* Rich polymorphism in nicotinamide revealed by melt crystallization and crystal structure prediction. *Commun Chem* **3**, (2020).
72. Chernov, A. A. & Pil'nik, A. A. Melt crystallization at large deviations from equilibrium. *Mater Today Proc* **16**, 144–150 (2019).
73. Lightowler, M. *et al.* Indomethacin Polymorph δ Revealed To Be Two Plastically Bendable Crystal Forms by 3D Electron Diffraction: Correcting a 47-Year-Old Misunderstanding**. (2021) doi:10.33774/chemrxiv-2021-s9fhf.
74. Chatterjee, J. N. Structure of the Anti-inflammatory Drug 4-Hydroxy-2-methyI-N-2-pyridyl-. **1**, 2948–2951 (1982).
75. Reck G 1, Dietz G , Laban G , Günther W , Bannier G, H. E. X-ray studies on piroxicam modifications. *Pharmazie* **43**, 477–481 (1988).
76. Reck, G. & Laban, G. Prediction and establishment of a new crystalline pyroxicam modification. *Pharmazie* **45**, 257–259 (1990).
77. Kuhnert-Brandstätter, M. & Porsche, U. Thermoanalytische und IR-spektroskopische Untersuchungen an polymorphen Acemetacin, Piroxicam, Propranololhydrochlorid und Urapidil. *Fresenius Z Anal Chem* **322**, 164–169 (1985).
78. Thomas, L. H., Wales, C. & Wilson, C. C. Selective preparation of elusive and alternative single component polymorphic solid forms through multi-component crystallisation routes. *Chemical Communications* **52**, 7372–7375 (2016).
79. Yao, C. *et al.* Polymorphism of Piroxicam: New Polymorphs by Melt Crystallization and Crystal Structure Prediction. *Cryst Growth Des* **20**, 7874–7881 (2020).
80. Alsarra, I. A., Al-Omar, M. & Belal, F. Valproic Acid and Sodium Valproate: Comprehensive Profile. *Profiles of Drug Substances, Excipients and Related Methodology* vol. 32 209–240 Preprint at https://doi.org/10.1016/S0099-5428(05)32008-9 (2005).
81. Nalivaeva, N. N., Belyaev, N. D. & Turner, A. J. Sodium valproate: an old drug with new roles. *Trends Pharmacol Sci* **30**, 509–514 (2009).
82. Alsarra, I. A., Al-Omar, M. & Belal, F. Valproic Acid and Sodium Valproate: Comprehensive Profile. *Profiles of Drug Substances, Excipients and Related*

Methodology vol. 32 209–240 Preprint at https://doi.org/10.1016/S0099-5428(05)32008-9 (2005).
83. Petruševski, G., Naumov, P., Jovanovski, G. & Ng, S. W. Unprecedented sodium-oxygen clusters in the solid-state structure of trisodium hydrogentetravalproate monohydrate: A model for the physiological activity of the anticonvulsant drug Epilim®. *Inorg Chem Commun* **11**, 81–84 (2008).
84. Day, G. S., Drake, H. F., Zhou, H. C. & Ryder, M. R. Evolution of porous materials from ancient remedies to modern frameworks. *Communications Chemistry* vol. 4 Preprint at https://doi.org/10.1038/s42004-021-00549-4 (2021).
85. Llewellyn, P. L., Rodriquez-Reinoso, F., Rouqerol, J., Seaton, N. & Maysl, T. J. *Studies in Surface Science and Catalysis 160 A New Classification of Pore Sizes*.
86. Dai, H. *et al.* Finned zeolite catalysts. *Nat Mater* **19**, 1074–1080 (2020).
87. Noro, S. I. *et al.* Porous coordination polymers with ubiquitous and biocompatible metals and a neutral bridging ligand. *Nat Commun* **6**, (2015).
88. Tan, K. T. *et al.* Covalent organic frameworks. *Nature Reviews Methods Primers* **3**, 1 (2023).
89. Suzuki, Y. & Hisaki, I. Structural details of carboxylic acid-based Hydrogen-bonded Organic Frameworks (HOFs). *Polymer Journal* vol. 56 1–16 Preprint at https://doi.org/10.1038/s41428-023-00840-2 (2024).
90. Foudazi, R., Zowada, R., Manas-Zloczower, I. & Feke, D. L. Porous Hydrogels: Present Challenges and Future Opportunities. *Langmuir* vol. 39 2092–2111 Preprint at https://doi.org/10.1021/acs.langmuir.2c02253 (2023).
91. Davis, M. E. *Ordered Porous Materials for Emerging Applications*. www.nature.com/nature (2002).
92. Furukawa, H. *et al.* Ultrahigh Porosity in Metal-Organic Frameworks. *Science (1979)* **329**, 424–428 (2010).
93. Yang, X. Y. *et al.* Hierarchically porous materials: Synthesis strategies and structure design. *Chemical Society Reviews* vol. 46 481–558 Preprint at https://doi.org/10.1039/c6cs00829a (2017).
94. Slater, A. G. & Cooper, A. I. Function-led design of new porous materials. *Science (1979)* **348**, aaa8075 (2015).
95. Zhang, Z., Lin, C. & Li, J. Utilization of Three-Dimensional Electron Diffraction for Structure Determination of Extra-Large-Pore Zeolites. *Small Methods* Preprint at https://doi.org/10.1002/smtd.202401461 (2024).
96. De Jong, K. P. & Koster, A. J. Three-dimensional electron microscopy of mesoporous materials - Recent strides towards spatial imaging at the nanometer scale. *ChemPhysChem* **3**, 776–780 (2002).
97. Weckhuysen, B. M. & Yu, J. Recent advances in zeolite chemistry and catalysis. *Chemical Society Reviews* vol. 44 7022–7024 Preprint at https://doi.org/10.1039/c5cs90100f (2015).
98. Ozin, G. A., Kuperman, A. & Stein, A. Advanced Zeolite, Materials Science. *Angewandte Chemie International Edition in English* vol. 28 359–376 Preprint at https://doi.org/10.1002/anie.198903591 (1989).
99. Sun, J. *et al.* The ITQ-37 mesoporous chiral zeolite. *Nature* **458**, 1154–1157 (2009).
100. Jiang, J. *et al.* Synthesis and Structure Determination of the Hierarchical Meso-Microporous Zeolite ITQ-43. *Science (1979)* **333**, 1131–1134 (2011).
101. Lin, Q.-F. *et al.* A stable aluminosilicate zeolite with intersecting three-dimensional extra-large pores. *Science (1979)* **374**, 1605–1608 (2021).
102. Li, J. *et al.* A 3D extra-large-pore zeolite enabled by 1D-to-3D topotactic condensation of a chain silicate. *Science (1979)* **379**, 283–287 (2023).

103. Gao, Z. R. *et al.* Interchain-expanded extra-large-pore zeolites. *Nature* **628**, 99–103 (2024).
104. Peng, D. X. Chemical mechanical polishing of steel substrate using aluminum nanoparticles abrasive slurry. *Industrial Lubrication and Tribology* **66**, 124–130 (2014).
105. Chen, G. *et al.* Alumina-Supported CoFe Alloy Catalysts Derived from Layered-Double-Hydroxide Nanosheets for Efficient Photothermal CO2 Hydrogenation to Hydrocarbons. *Advanced Materials* **30**, (2018).
106. Haar, S., Schrader, E. & Gatewood, B. M. Comparison of Aluminum Mordants on the Colorfastness of Natural Dyes on Cotton. *Clothing and Textiles Research Journal* **31**, 97–108 (2013).
107. Temuujin, J. *et al. Thermal Formation of Corundum from Aluminium Hydroxides Prepared from Various Aluminium Salts*. *Bull. Mater. Sci* vol. 23 (2000).
108. Mann, V. S. & Pandey, O. P. Effect of Dual Particle Size Corundum Particles on the Tribological Properties of LM30 Aluminium Alloy Composites for Brake Rotor Applications. *Arab J Sci Eng* **46**, 12445–12463 (2021).
109. Hu, G., Wang, N., O'Hare, D. & Davis, J. Synthesis of magnesium aluminium layered double hydroxides in reverse microemulsions. *J Mater Chem* **17**, 2257–2266 (2007).
110. Evans, H. A. *et al. Aluminum Formate, Al(HCOO) 3 : An Earth-Abundant, Scalable, and Highly Selective Material for CO 2 Capture*. *Sci. Adv* vol. 8 https://www.science.org (2022).
111. Lenzen, D. *et al.* Scalable Green Synthesis and Full-Scale Test of the Metal–Organic Framework CAU-10-H for Use in Adsorption-Driven Chillers. *Advanced Materials* **30**, (2018).
112. Achenbach, B. *et al.* Unlocking the Chemical and Structural Complexity of Aluminum Hydroxy Acetates: from Commodity Chemicals to Porous Materials. *Chemistry - A European Journal* (2024) doi:10.1002/chem.202403634.
113. Rao, C. N. R., Natarajan, S. & Vaidhyanathan, R. Metal carboxylates with open architectures. *Angewandte Chemie - International Edition* vol. 43 1466–1496 Preprint at https://doi.org/10.1002/anie.200300588 (2004).
114. Hood, G. C., Ihde Vol, A. J., George Hood, B. C. & Ihde, A. J. *Aluminum Acetates and Propionates-Their Preparation and Composition1*. *J. Phys. Colloid Chem* vol. 103 https://pubs.acs.org/sharingguidelines (1934).
115. Lukic, M. *et al.* Formulation of topical acidic products and acidification of the skin – Contribution of glycolic acid. *Int J Cosmet Sci* **43**, 419–431 (2021).

Jiaoyan Xu
was born in Shandong, China. She obtained her Bachelor's and Master's degrees from Qingdao University, China. She started her PhD at Stockholm University in 2020. She has expertise in electron crystallography.

ISBN 978-91-8107-198-6

Department of Chemistry

Stockholm University